Article

Mechanism of Laser-Induced Bulk and Surface Defect Generation in ZnO and TiO2 Nanoparticles: Effect on Photoelectrochemical Performance

Marcus Lau, Sven Reichenberger, Ina Haxhiaj, Stephan Barcikowski, and Astrid M Müller

ACS Appl. Energy Mater., **Just Accepted Manuscript** • Publication Date (Web): 06 Sep 2018

Mechanism of Laser-Induced Bulk and Surface Defect Generation in ZnO and TiO_2 Nanoparticles: Effect on Photoelectrochemical Performance

Marcus Lau[†,§], Sven Reichenberger[†], Ina Haxhiaj[†,||], Stephan Barcikowski*[†], Astrid M. Müller*[‡¶]

[†]Technical Chemistry I, Department of Chemistry, and Center for Nanointegration Duisburg-Essen (CENIDE), University of Duisburg-Essen, Universitätsstraße 7, 45141 Essen, Germany

[‡]Beckman Institute, California Institute of Technology, 1200 E California Blvd., Mail Code 139-74, Pasadena, CA 91125, USA

*E-mail: stephan.barcikowski@uni-due.de, astrid.mueller@rochester.edu

KEYWORDS: pulsed laser processing, defect density, photoelectrochemistry, zinc oxide, titanium dioxide

ABSTRACT: Laser processing of neat and gold-nanoparticle-functionalized ZnO and TiO_2 nanoparticles by nanosecond-355-nm or picosecond-532-nm light enabled control of photocurrent generation under simulated sunlight irradiation in neutral aqueous electrolytes. We obtained more than two-fold enhanced photoelectrochemical performance of TiO_2 nanoparticles upon irradiation by picosecond-532-nm pulses that healed defects. Laser processing and gold nanoparticle functionalization of ZnO and TiO_2 nanomaterials resulted in color changes that did not originate from optical bandgaps or crystal structures. Two-dimensional photoluminescence data allowed us to differentiate and quantify surface and bulk defects that play a critical yet oft-underappreciated role for photoelectrochemical performance as sites for detrimental carrier recombination. We developed a detailed mechanistic model of how surface and bulk defects were generated as a function of laser processing parameters and obtained key insights on how these defects affected photocurrent production. The controlled healing of defects by pulsed-laser processing may be useful in the design of solar fuels materials.

Photoelectrochemical water splitting by earth-abundant materials has attracted much interest as a solution to the world's energy crisis.[1-3] Non-precious transition metal oxides, such as ZnO or TiO_2, are suitable semiconductor materials for photocatalytic water splitting.[4-6] In spite of reported successes with ZnO and TiO_2 photoanodes, sunlight-driven current generation must be improved for use in a functional water-splitting device. Such advances require a deep understanding of the photophysical properties of these materials; of particular importance is the effect of bulk and surface defects on photoelectrochemical performance.[7,8]

We systematically varied bulk and surface defect densities in ZnO and TiO_2 nanoparticles by two laser processing protocols, using a homebuilt liquid-jet reactor (Figure S1): laser-irradiation by nanosecond 355-nm pulses (ca. 65 mJ cm^{-2}, for efficient particle melting)[9,10] or by picosecond 532-nm pulses (ca. 30 mJ cm^{-2}, for efficient particle fragmentation).[11]

We also irradiated composites that consisted of ZnO or TiO_2 nanoparticles with adsorbed laser-made plasmonic gold nanoparticles (AuNPs), to shed further light on the mechanisms of defect generation in ZnO and TiO_2 nanoparticles upon laser processing. Enhancement of photocatalytic activities by AuNPs on thin film TiO_2 and hot pressed TiO_2-Fe_2O_3 nanoparticle structures have been described.[12,13] Overall, we prepared seventy materials (Figure 1) and assessed optical bandgaps, crystal phases, and surface and bulk defect densities. We measured photocurrent generation of our materials in aqueous electrolytes under virtually identical conditions as a function of laser processing parameters, to ensure comparability.

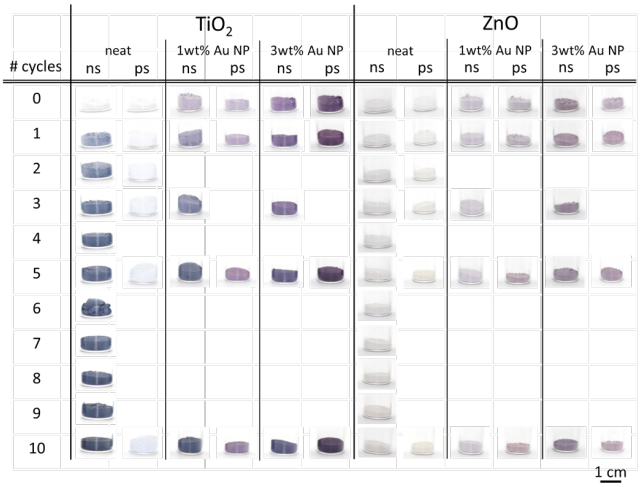

Figure 1: Photos of laser-modified nanoparticles. The materials were irradiated by 355 nm, 40 ns, 228 µJ, 85 kHz, ca. 65 mJ cm^{-2} pulses (ns columns) or by 532 nm, 10 ps, 75 µJ, 100 kHz, ca. 30 mJ cm^{-2} pulses (ps columns) in free liquid jets. Depicted are neat TiO_2 and ZnO photoanode materials, or with two nominal amounts of pre-irradiation-physisorbed AuNPs; all materials were subjected to different laser energy doses (see SI for conversion of number of cycles into mass-specific energy dose).

Pulsed lasers are powerful tools for the time-efficient preparation and/or modification of functional materials.[14-21] Recent investigations have shown that laser-modified TiO_2 particles can be used to improve the light-driven water splitting to form hydrogen[22] or

rhodamine B degradation.[23] Irradiation by ns-532-nm pulses yielded sub-micrometer TiO_2 spheres, SMS.[22] The materials appeared bluish, consisted of sub-oxide Magnéli phases, and exhibited enhanced light-driven hydrogen formation from water.[22] Since the first reports on laser melting of particles in liquids,[24-26] more mechanistic details of SMS generation have been obtained: experiments have demonstrated that laser fluence was crucial for SMS production, in agreement with theoretical predictions. [9, 27] Pulsed laser melting in liquids (PLML) does not only permit fluence-controlled reduction of metal oxidation states,[25] but it also provides access to new material combinations.[10]

Besides melting, laser irradiation of particles in liquids can result in fragmentation. In contrast to PLML, pulsed laser fragmentation in liquids (PLFL) requires higher fluences, typically above ca. 40 – 100 mJ cm^{-2}.[10, 11]

Pulse length plays a role too: Nanosecond lasers are known to cause thermal particle size and shape modifications, whereas pulses with durations of up to a few picoseconds mainly produce non-thermal response at sufficiently high laser fluences.[28, 29] The reason for the effect of pulse duration on particle generation is that the pulse length affects the temperature of the electron gas and solid lattice (of the target) and, hence, the chemical potential and thermal load, respectively, according to the two-temperature model.[30] Therefore, nanosecond lasers are known to cause thermally mediated modifications of structure, particle size, and shape. In contrast, pulses with durations that are comparable to the electron-phonon-relaxation time (up to a few picoseconds) mainly induce high electron temperatures while the lattice remains cold, thereby causing non-thermal responses, such as electron spillage, electrostatic particle fission (Coulomb explosion), or lattice disordering, depending on the applied laser fluences.[31]

Importantly, both processes, PLML and PLFL, have been shown to generate defects in the particle bulk that can improve the photocatalytic activity of anatase and rutile TiO_2.[32] Surface defects also play a key role for water splitting mediated by TiO_2.[33] Besides defects, modification of the optical bandgap improved the light-driven water-splitting performance of TiO_2.[34] Doping, such as by nitrogen of ZnO,[35] by carbon of TiO_2,[36] or hydrogen treatment of TiO_2,[37] enhanced photocurrents. And the effect of ball-milling time on ultraviolet-light-induced degradation of methylene blue at ZnO and TiO_2 powders has recently been reported.[38] Another interesting route to advance photoanode materials is the utilization of plasmonic effects. Improvement of TiO_2[39-41] and ZnO[42] water splitting performance by plasmonic gold nanoparticles has been observed.

Enhancement of photocatalytic activity requires that deleterious recombination of charge carriers, e.g. at defect sites, must be minimized.[43] Carrier diffusion path lengths may limit catalytic activity, highlighting the importance of nanostructuring.[44, 45] Surface modifications were found to enhance PEC performance by passivation of surface states.[46] Carrier concentrations and non-radiative recombination rates also mattered.[47] Meyer et al. reported electrical and optical properties of porous nanocrystalline TiO_2 films and found that charge accumulated in Ti^{3+} trap states.[48] Jaramillo et al. described hierarchically branched TiO_2 nanorod structures with enhanced carrier collection efficiency.[49] Marschall et al. prepared TiO_2 nanoparticle multiphase heterojunctions from ionic liquids that beneficially impacted charge carrier separation at interphase connections.[50] And Gamelin et al. reported that electron confinement in nanosized ZnO quantum dots led to delocalized electrons that behaved like conduction band electrons.[51] Similarly, charge carrier separation was significantly enhanced in the presence of adsorbed nanoparticles, resulting in improved photocurrent generation.[52]

Here, we combined gold nanoparticle adsorption with modifications of TiO_2 and ZnO particles by laser irradiation and tested photocurrent generation as a function of laser process parameters, optical bandgap, crystal phase, and defect density. We developed a detailed model of how bulk and surface defects were generated and how they affected the photoelectrochemical performance of our laser-modified ZnO and TiO_2 materials.

Results and Discussion

We prepared seventy materials to systematically study the effects of laser parameters or the presence of adsorbed gold nanoparticles during laser treatment and concomitant changes to bandgap, crystal structure, and bulk and surface defect densities on photocurrent generation of ZnO and TiO_2 photoanodes under simulated sunlight irradiation in neutral aqueous electrolytes. We observed unambiguous color changes of the ZnO and TiO_2 nanoparticles as a function of laser irradiation and/or AuNP functionalization (Figure 1) and were interested in (1) the physical origin of the individual colors, and (2) how pulsed-laser processing affected photoelectrochemical performance.

For clarity, we first describe the photophysical and structural properties ZnO materials, followed by TiO_2 nanoparticles, and finally close this section with a correlation of surface and bulk defects to photocurrent generation.

ZnO Materials

We measured the optical spectra of all ZnO preparations in diffuse powder reflection mode (Figure S2), followed by Kubelka-Munk analysis. We derived bandgaps by extrapolation of the absorption regime with linear increase. Pre-irradiation adsorption of AuNPs increased absorptions in the visible range, presumably due to AuNP plasmon resonances. We did not find significant changes of bandgaps as a function of applied laser irradiation or AuNP loading (Figure 2). We found the average ZnO bandgap was ca. (3.25 ± 0.01) eV, in agreement with reported values.[53]

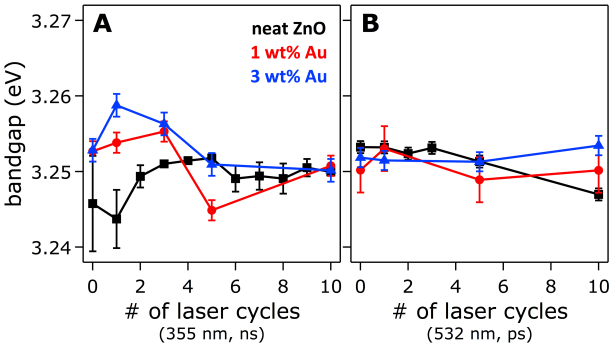

Figure 2: Optical bandgaps of neat ZnO particles (black squares), ZnO with nominally 1 (red circles) or 3 wt % (blue triangles) AuNPs, laser-irradiated by ns-355-nm (A) or ps-532-nm (B) pulses.

We collected XRD data to assess if laser irradiation and/or AuNP functionalization led to structural changes in ZnO upon laser treatment. We assigned the detected XRD patterns to wurtzite ZnO (PDF 36-1451; ICDD, 2012); no other crystal phases were present. Importantly, we found that the ZnO reflections did not

change as a function of laser irradiation or AuNP functionalization (Figure 3 and SI).

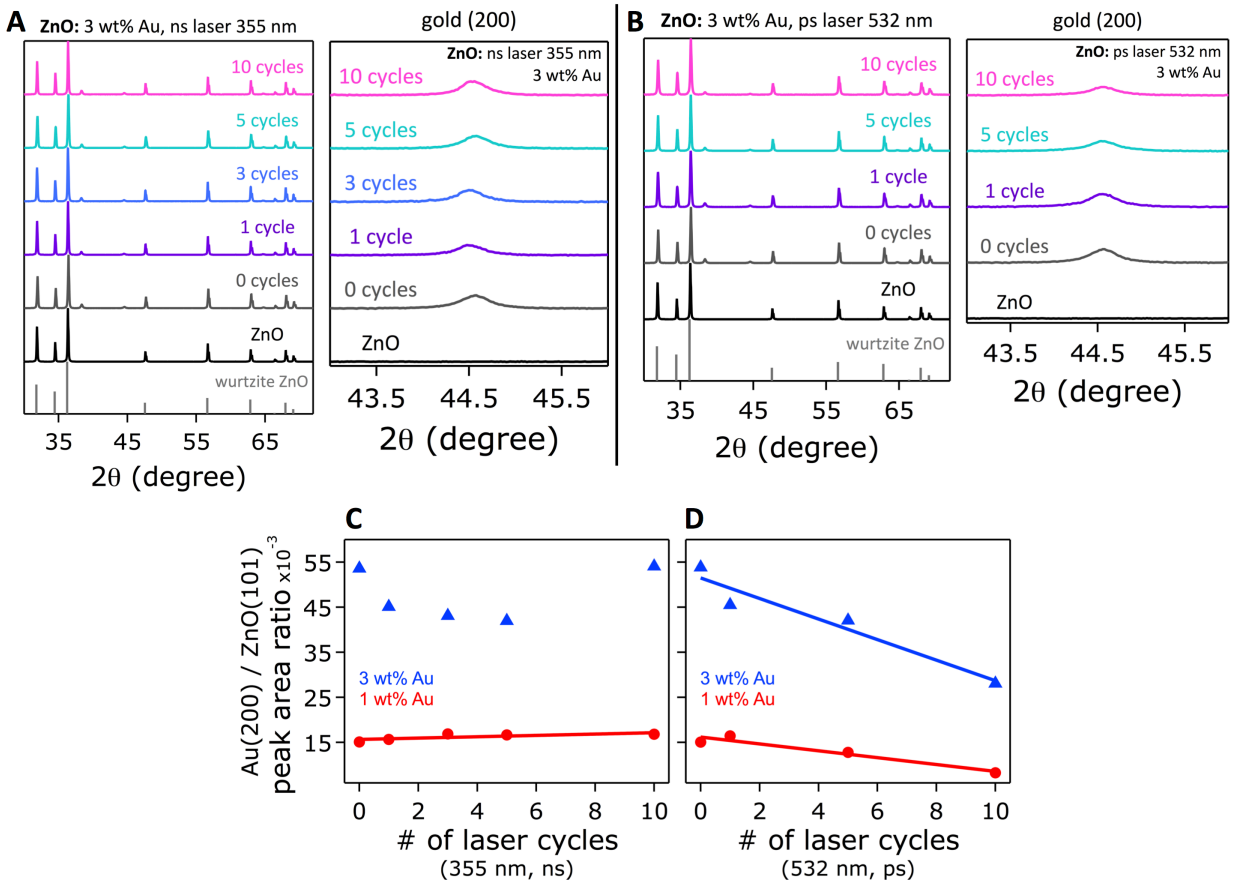

Figure 3: XRD data of ZnO loaded with nominally 3 wt% AuNP as a function of laser irradiation by ns-355-nm (A) or ps-532-nm (B) pulses. Also shown are relative Au/ZnO peak area ratios (C, ns-355-nm pulses; D, ps-532-nm pulses) that indicate how much gold remained on the ZnO particles after laser treatment of ZnO–AuNP composites with nominally 1 (red circles) or 3 wt% (blue triangles) AuNPs; the lines are linear fits.

Wurtzite is the thermodynamically most stable polymorph of ZnO.[54] Since the XRD reflections remained virtually unaltered as a function of laser processing, we conclude that our laser fluences were not far from or within the thermodynamic equilibrium below the threshold for bulk restructuring. Our findings are in agreement with results on laser-generated ZnO by millisecond laser ablation (operating in the thermal equilibrium regime) and pulsed laser deposition experiments, in which wurtzite was the predominantly formed crystalline species.[55, 56]

We detected an additional reflection at ca. 44.5° in ZnO materials that were immersed in laser-generated AuNP colloids prior to laser treatment, attributable to Au(200). Quantification of this Au signal revealed how laser irradiation of ZnO–AuNP composites affected the AuNPs on ZnO. The Au(200)/Au(111) ratio remained constant, suggesting that AuNP faceting did not play a role in the detected changes of the Au(200) reflection; the Au(111) reflection appeared at 38.4°. We integrated the Au(200) peak and normalized it to the peak area of the ZnO reflection with highest intensity, ZnO(101), to obtain the relative amount of Au(200) per preparation (Figure 3 C and D). We found that ns-355-nm irradiation of ZnO–AuNP composites with nominally 1 wt% Au did not result in significant changes of the relative Au(200) signal. For materials with nominally 3 wt% Au, we observed a U-shaped dependence. Less gold was detectable as the energy dose rose, and only ZnO irradiated at the highest dose exhibited a gold amount that was similar to that of un-irradiated ZnO (Figure 3 C). We explain this U-shaped dependence by an energy-dose-dependent combination of laser-induced AuNP detachment, i.e. gold loss, and inclusion of AuNPs into ZnO at high ns-355-nm energy doses, in line with previous results,[10] that counteracted gold loss.

We obtained different trends with ps-532-nm pulses: Irrespective of the AuNP colloid concentration, the amount of gold that was detectable on ZnO linearly decreased with increasing irradiation dose, more so for nominally 3 than 1 wt% Au (Figure 3 D). Our results indicate that ps-532-nm pulses caused laser-induced detachment of gold from ZnO–AuNP composites, in line with reports on nanoparticle stripping from surfaces by laser irradiation due to plasma-induced shock; this surface purification technique has found use in semiconductor technology applications. [57-59] Absorption cross sections of AuNPs are significantly higher at 532 than 355 nm.[60] Conservation of mass dictates that the detached gold must remain within the laser-preparation vessel. Most likely, this laser-detached gold adsorbed to the glass walls of this vessel, as suspended AuNPs would readily re-adsorb onto ZnO. We observed a linear dependence of gold loss as a function of ps-532-nm laser cycles (Figure 3 D), suggesting that gold loss scaled with the number of contacts the irradiated ZnO–AuNP composite suspension had with the glass walls of the laser-preparation vessel. Fragmentation of AuNPs by 532-nm laser pulses[30, 60-62] could also be at

play, but the laser fluences used here were too low to explain the gold loss by fragmentation.[60]

Our observed absence of changes in bandgaps (Figure 2) and crystalline structure (Figure 3) suggests that the color changes we detected in ZnO materials upon laser irradiation (Figure 1) must have a different origin.

We turned to photoluminescence (PL) experiments that reveal information on bulk and surface defect densities to explain the observed color changes and AuNP physisorption characteristics of laser-irradiated ZnO particles. We excited our materials by UV light in the range of 290 – 390 nm and collected the emission in two-dimensional (2D) fashion as a function of the excitation wavelength. We did not detect any PL signal with excitation wavelengths >390 nm. A graph of 2D PL data of un-irradiated neat ZnO is shown in Figure 4; 2D PL data of all other ZnO preparations are shown in Figures S5 and S6.

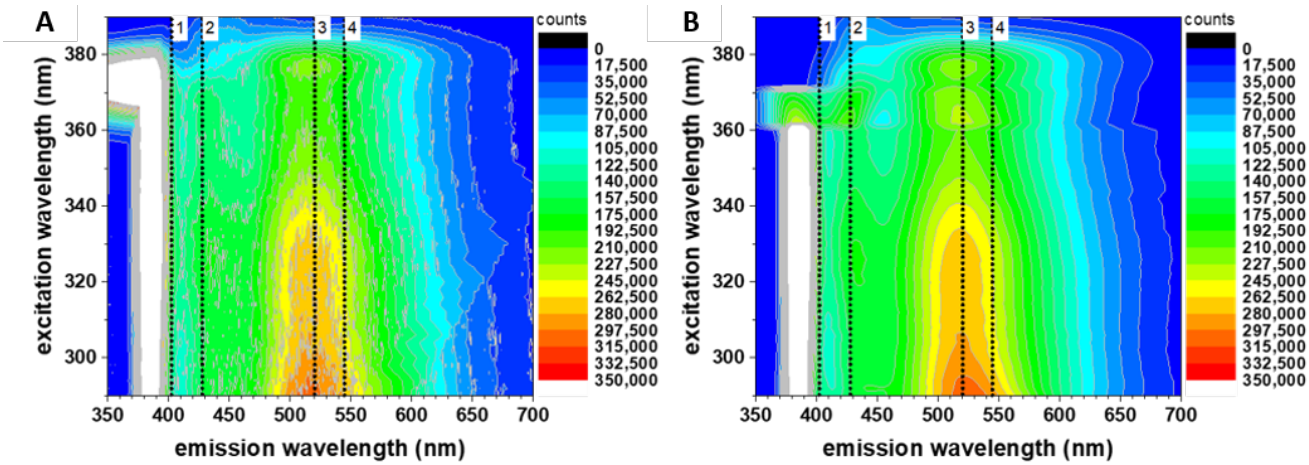

Figure 4: 2D PL raw data (A) and simulation (B) of un-irradiated neat ZnO particles; data processing details are in the SI. The dotted lines indicate optically active defects used for the fitting process.

In addition to strong bandgap PL centered at ca. 385 nm (3.22 eV) attributable to excited electrons near the band edge,[63, 64] we observed a green emission, in agreement with previous reports.[63, 65-69] We chose the *z*-scale of the graphs such that weaker emissions are visible; as a result the strong bandgap emission appears white.

The origin of the blue-green PL has been controversially discussed in the community. This PL in ZnO has been ascribed to the presence of impurities,[70] or oxygen[71-73] or zinc[67-69, 73-75] based defects. A recent report aimed at distinguishing Zn from O defects explained the blue-green emission by oxygen features present in zinc vacancies that stemmed from dangling oxygen bonds and induced an oxygen-like defect character of zinc vacancies.[74] Red luminescence (at ca. 655 nm) has been assigned to true oxygen vacancies using PL and electron paramagnetic resonance (EPR) data.[68] This red PL is consistent with the reported transition energy of the oxygen vacancy donor state located at 1.8 eV (688 nm).[67] We did not detect significant emission in the orange-red spectral region (Figure 4 and SI).

Annealing of ZnO in oxygen-rich atmosphere has been predicted to predominantly form oxygen interstitials and/or zinc vacancies[67, 76]; these Zn vacancies are thought to give rise to the observed blue-green PL.[53, 69, 74, 75] Formation of oxygen vacancies, zinc interstitials and antisite defects is unlikely due to high formation energies above 6 eV in such oxygen-rich conditions.[67, 76]

We assign the blue-green PL to zinc vacancies, in line with reported work.[53, 69, 74] Oxidation processes during pulsed-laser ablation in liquids or pulsed-laser post-processing have been observed.[15, 62, 77, 78] In ZnO–AuNP composites, formation of oxygen interstitials may be favored in close proximity to the AuNP[76] due to a reduced Fermi level caused by electron transfer from ZnO to the AuNP.[79] Interstitial defects have been reported to exhibit low diffusion barriers in ZnO.[67, 80] As a result, fast curing of oxygen interstitials, which may have formed directly after laser treatment, is likely, especially at ZnO–AuNP interfaces. Note that we collected PL data weeks after we laser processed our materials. Moreover, since we did not observe any additional PL signals in ZnO–AuNP composites compared to neat ZnO (Figure S5 and S6), we rule out oxygen interstitials as PL centers.

Two different types of zinc vacancies (type I and II) have been identified by positron annihilation spectroscopy (PAS).[69, 81] The Zn vacancies exhibited emissions at 536 nm (2.31 eV, type I, below 600 °C) and 501 nm (2.47 eV, type II, above 600 °C).[69] Janotti and Van de Walle performed DFT calculations on point defects in ZnO and reported two charge-state transitions for Zn vacancies with energy levels at 0.18 eV, $V_{Zn}^{(0/-)}$, and 0.87 eV, $V_{Zn}^{(-/2-)}$, below the bandgap.[67] Based on these findings we deconvoluted our observed blue-green PL signal using four contributions: type I and type II Zn vacancies with two separate transitions per type at 0.18 eV and 0.87 eV below the bandgap.

We found a constant bandgap of 3.25 eV (Figure 2). Therefore, in line with ref. 67, we assign PL at 404 nm (3.07 eV, #1 in Figure 4) to type II $V_{Zn}^{(0/-)}$ and PL at 521 nm (2.38 eV, #3 in in Figure 4) to type II $V_{Zn}^{(-/2-)}$. We detected two additional signals at 428 and 544 nm during the fitting process (#2 and #4 in Figure 4); good fits required the inclusion of this additional red-shifted peak pair that we ascribe to type I zinc vacancies. In summary, we assign the four distinguishable signals to type I and type II Zn vacancies with separate $V_{Zn}^{(0/-)}$ and $V_{Zn}^{(-/2-)}$ transitions (Table 1).

Table 1: Optically active defects in ZnO and associated emission wavelengths and photon energies.

Origin of PL	Type of transition	Emission wavelength (nm)	Photon energy (eV)
Bandgap recombination [63, 64]	–	385	3.22
$V_{Zn}(II)$[69]	$V_{Zn}^{(0/-)}$	404	3.07 (E_g – 0.18 eV)[67]
$V_{Zn}(I)$[69]	$V_{Zn}^{(0/-)}$	428	2.90
$V_{Zn}(II)$[69]	$V_{Zn}^{(-/2-)}$	521	2.38 (E_g – 0.87 eV)[67]
$V_{Zn}(I)$[69]	$V_{Zn}^{(-/2-)}$	544	2.28

We modeled our 2D PL spectra as a function of emission wavelength by a global fit function that consisted of five Gaussians, with the aim to deconvolute PL contributions attributable to emissions from bandgap states and individual defect types. The centers of these Gaussians were constrained to the wavelengths given in Table 1, with a variation of ± 2 nm, as we used a 2-nm bandpass during data acquisition. We stepped the excitation wavelengths in 2-nm increments. For our fitting, we integrated the peak intensities, which were recorded at each individual excitation wavelength, over the entire excitation range (290 – 390 nm). More details regarding data processing and fitting are in the SI. The fits matched the 2D PL data well and allowed us to quantify zinc vacancy defect contributions. The $V_{Zn}^{(0/-)}$ and $V_{Zn}^{(-/2-)}$ transitions in each Zn vacancy type originate from the same defect centers.[69] We obtained two separate PL contributions for type I and type II Zn vacancies by adding integrated peak intensities of $V_{Zn}^{(0/-)}$ and $V_{Zn}^{(-/2-)}$ transitions for each type, denominated $V_{Zn}(I)$ and $V_{Zn}(II)$. The results as a function of material preparation are shown in Figure 5.

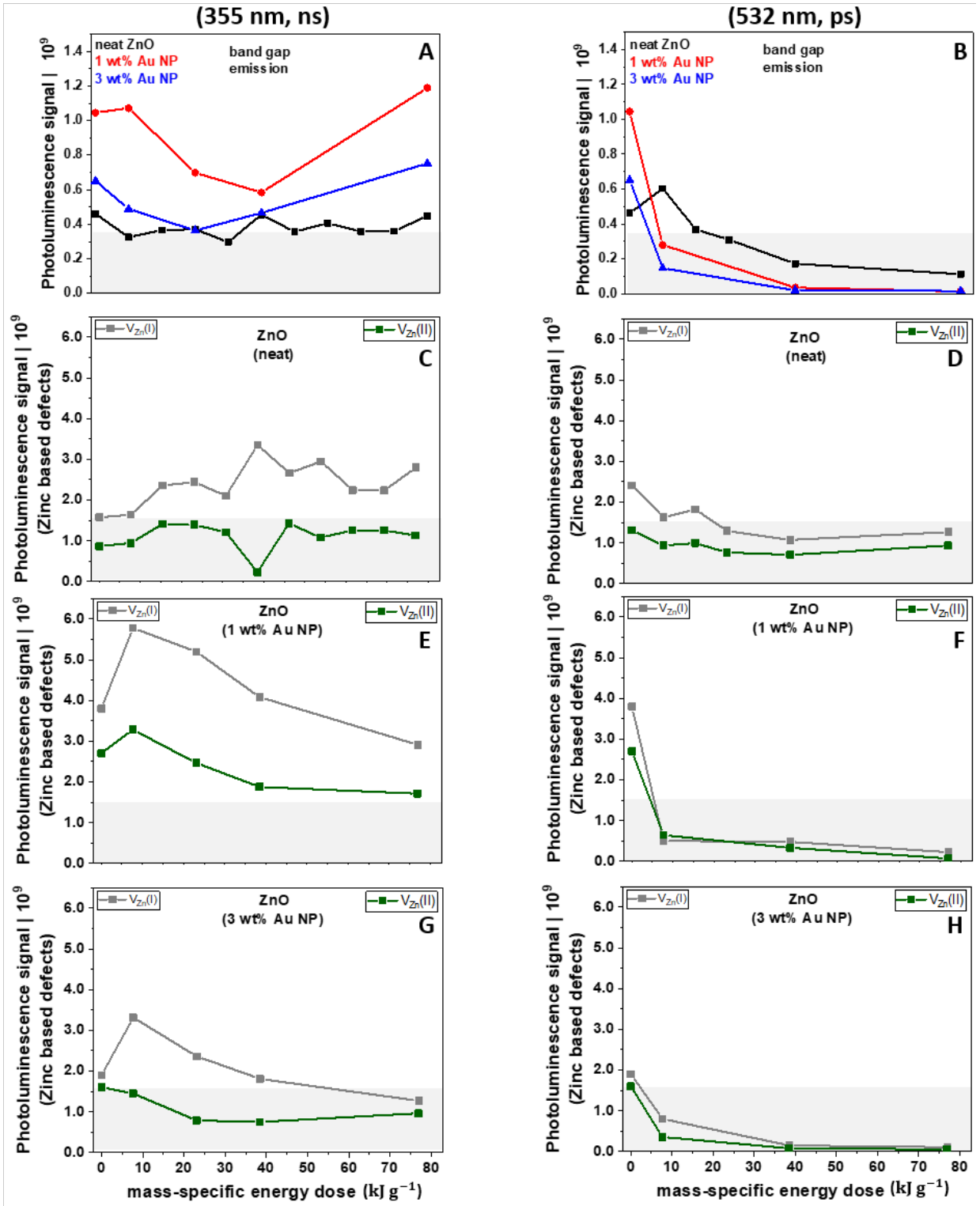

Figure 5: Contributions of bandgap states (A, B) and different ZnO defects to the measured PL signal as a function of material preparation, i.e. laser type and irradiation energy dose. ZnO particles were irradiated by ns-355-nm (left) or ps-532-nm (right) pulses; neat ZnO (C, D), ZnO with nominally 1 (E, F) or 3 wt% (G, H) AuNPs. Lines are included to guide the eye. The gray background serves as a reference to aid visual comparisons of panels.

We did not observe significant changes in bandgap emissions of neat ZnO particles that were irradiated by ns-355-nm pulses, irrespective of energy dose (Figure 5 A, black squares). ZnO–AuNP composites showed enhanced bandgap emission with nominally 1 wt% Au (Figure 5 A, red circles). Materials with nominally 3 wt% Au exhibited bandgap emissions similar to those of neat ZnO. We obtained similar trends in emission intensities as a function of gold loading for individual defect contributions as for bandgap states (Figure 5 C, E, and G).

Enhanced bandgap PL upon AuNP adsorption (Figure 5 A) has been reported and was attributed to synergetic electronic effects, such as near-field-mediated plasmon coupling, between nanoparticle and support materials.[63, 64] Other work described PL quenching as a function of increased AuNP loading.[63, 65, 66] Zhang et al. discussed PL quenching as a result of a combination of surface plasmon enhancement effects (local amplification of the incident field) by adsorbed AuNPs and a quenching effect via direct energy transfer (damping of dipole oscillations) between ZnO and gold.[63] In their study, the authors used insulating Al_2O_3 layers of varying thickness that laterally separated ZnO and AuNP surfaces; this way, they were able to demonstrate that damping occurred when ZnO and AuNP were in direct contact.[63] Damping weakened with increasing separation distance, whereas plasmon enhancement was active even at large separations of up to 30 – 40 nm.[63] In our work, the surfactant-free laser-generated AuNPs were in direct contact with the ZnO particles, as depicted in Figure 6.

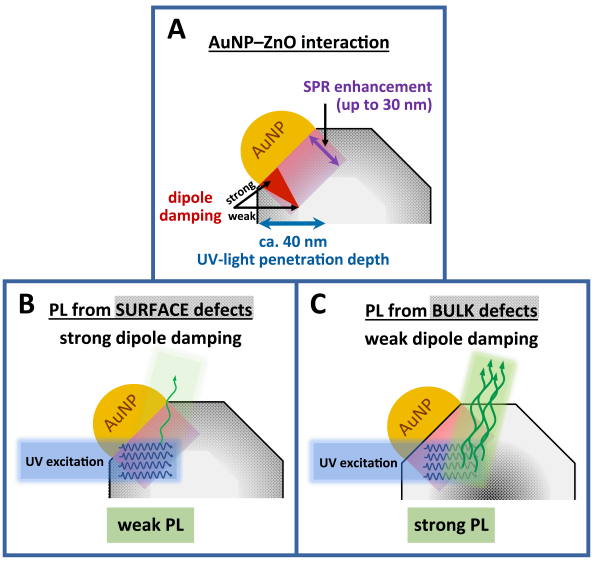

Figure 6: Illustration of the physical origins of the different PL intensities that we observed in ZnO–AuNP composites as a function of laser irradiation dose. Different electric field contributions arise from the interaction of the AuNP with the transition metal oxide support, shown in A, adapted from ref. 63. The penetration depth of UV light is ca. 40 nm in ZnO.[82] Upon irradiation with UV light, e.g. by the excitation source in our PL studies, the surface-plasmon resonance (SPR) of the AuNP induces an electric field enhancement that reaches up to 30 nm into ZnO,[63] whereas the dipole oscillation damping is strongest within the first few surface layers.[63] SPR field enhancement amplifies PL, and dipole oscillation damping attenuates PL.[63] Hence, defect PL from the bulk is strong (B), whereas defect PL from sites at or near the transition metal oxide support surface is weak due to short-range dipole oscillation damping (C).

We reconcile our results on ZnO–AuNP composites that had ZnO and gold in direct contact with Zhang et al.'s findings by consideration of the location of defects as a function of laser treatment, i.e. within the ZnO bulk or at the surface. We expect little dampening but much plasmon enhancement, ergo strong PL, if the ZnO–AuNP composite material exhibits high bulk but low surface defect densities (Figure 6 C). Albeit counterintuitive, the scenario of few surface defects, while the majority of defects is located in the bulk, is comparable to a high separation distance in ref. 63. If, however, the majority of defects is located near or at the ZnO surface we anticipate strong damping of dipole oscillations and concomitant low PL (Figure 6 B), comparable to small Au–ZnO separations described in ref. 63. Additionally, AuNPs are able to absorb the PL excitation light, according to Mie theory, and green emission light due to their plasmon resonance (Figure 5 C – F).[63, 64, 83] This parasitic light absorption by AuNPs explains the observed loss in PL intensity with higher AuNP loading.

We found that ns-355-nm laser processing of ZnO particles altered the densities and blue-green emission of zinc vacancy defects with increasing laser energy dose: PL signals for $V_{Zn}(I)$ slightly increased whereas those for $V_{Zn}(II)$ remained constant in neat ZnO (Figure 5 C). Comparison of PL data of neat ZnO with those of ZnO–AuNP composites with nominally 1 wt% Au (Figure 5 C and E, both irradiated by ns-355-nm pulses) allowed us to assign the location of the laser-generated type I zinc vacancies, $V_{Zn}(I)$, as primarily within the ZnO bulk. At low ns-355-nm laser energy dose, we obtained higher $V_{Zn}(I)$ PL intensities for ZnO–AuNP composite nanoparticles than for neat ZnO. As mentioned above, strong PL intensities of ZnO–AuNP composites are indicative of high bulk defect densities, where dipole damping is low but SPR enhancement is very pronounced (Figure 6). At higher energy doses, we observed regeneration or diffusion of $V_{Zn}(I)$ defects to the surface in ZnO–AuNP composites with 1 or 3 wt% AuNP. We note that Lau et al. have described isochoric melting of neat ZnO, including formation of spherical particles during ns-355-nm laser irradiation at high energy doses; at energy doses comparable to the present work, only minor changes to the ZnO particle shape were previously detected.[10] But isochoric melting may benefit defect mobility, diffusion, and curing.

Our observation of zinc vacancy defect regeneration in ZnO–AuNP composites upon irradiation by ns-355-nm pulses with high energy doses is in agreement with reported Zn vacancy formation. Positron annihilation experiments of high-temperature-calcinated ZnO (550 °C) by Wang et al.[69] and time-correlated single photon counting experiments of ZnO that was calcinated at 900 °C by Kavitha et al. [86] evidenced Zn vacancy formation. We explain our results by AuNP-supported isochoric melting of ZnO by ns-355-nm laser treatment, consistent with refs. 10 and 11.

We obtained a different picture for laser irradiation of ZnO particles by ps-532-nm pulses (Figure 5, right). We found the bandgap emission intensity decreased for all three materials (neat ZnO, or ZnO with nominally 1 or 3 wt% Au) as a function of laser energy dose (Figure 5 B). We observed similar results for defect emissions (Figure 5 D, F, and H): Laser treatment of neat ZnO led only to small changes of the defect structure; the contributions of both defect centers only slightly decreased. We surmise that ps-532-nm pulses induced only a small driving force (e.g. thermal load) in ZnO, consistent with the small absorption cross section of ZnO at 532 nm (Figure S2); the absorptivity of ZnO at 532 nm is ca. 2 – 3 orders of magnitude smaller than that at 355 nm.[87] Kavitha et al. attributed the absorption of green light (532 nm) to prevalent zinc vacancies.[86] Our data (Figure 5 C and D, at 0 kJ g^{-1}) suggest that such zinc vacancy defects existed in our neat ZnO nanoparticles before laser processing, similar to ref. 86. Thus, we infer that energy transfer of 532-nm pulses to ZnO occurred near preexisting defect sites that occupy energy states within the bandgap. PL data analysis showed that the defect density shown in Figure 5 C did not significantly change upon ps-532-nm laser treatment of neat ZnO, suggesting that ps-532-nm laser pulses primarily altered the preexisting defect structure instead of creating new defects.

Our ZnO–AuNP composites exhibited strong quenching of defect PL, even with the lowest applied ps-532-nm energy dose, consistent with the mechanism shown in Figure 6. High surface defect densities and parasitic absorption of excitation and emitted light by AuNPs led to low PL. We observed the largest decrease of PL intensity after one laser cycle, followed by a less steep decrease at higher energy doses (Figure 5 F and H), indicating diffusion of bulk defects towards the ZnO surface. Upon excitation by green light, such as the 532-nm pulses used here, the strong plasmon resonance of AuNPs can cause near-field enhancements[12] that may facilitate electron transport and concomitant defect formation and/or diffusion. Hot electron injection from AuNPs to semiconductor supports has also been discussed.[88-90]

Our results point to two different defect modification mechanisms, depending on irradiation laser properties: Nanosecond 355-nm pulses induced massive thermal loads within the ZnO nanoparticles, as the UV light was strongly absorbed by ZnO; 355-nm photons have an energy of 3.49 eV, which is well above the bandgap of ZnO (3.25 eV, Figure 2), giving rise to strong absorption, independent of the defect density before laser irradiation. Additionally, the long pulse length of 40 ns was 4 orders of magnitude larger than typical electron-phonon-relaxation times (ca. 0.5 ps).[91] As a result, we expect a thermal equilibrium between electron temperature and lattice temperature, according to the two-temperature model.[61] Therefore, only moderate electron temperatures exist, but isochoric melting occurs, which causes bulk defects to emerge during the cooling process. Our results on ns-355-nm-irradiated ZnO–AuNP composites provide further evidence for isochoric melting of ZnO.

Our ps-532-nm laser generated pulses with a duration of 10 ps, which is only one order of magnitude longer than typical electron-phonon-relaxation times.[91] Together with the low absorption coefficient of ZnO at 532 nm,[87] we expect low thermal load in the bulk, but significantly higher local electron temperatures compared to ns-355-nm laser pulses.[61] Additionally, because of the non-linear, defect-mediated absorption characteristics of ZnO, absorption of 532-nm photons predominantly occurred at intra-bandgap electronic states attributable to preexisting defect sites. If the intrinsic defect density is low, such as in our un-irradiated neat ZnO particles,[86] few light–matter interactions occur; hence, we observed less pronounced changes in PL intensities and concomitant defect densities than with ns-355-nm pulses. Moreover, ps-532-nm-irradiated ZnO–AuNP composites exhibited low PL intensities due to strong dipole damping by AuNPs; the PL intensity decrease was most pronounced after the first laser cycle. Our results suggest defect diffusion towards the ZnO surface.

TiO_2 Materials

We obtained even more pronounced color changes in TiO_2 nanoparticles than in ZnO materials (Figure 1). Analogous to our approach with ZnO, we determined the bandgaps of all our TiO_2 preparations (Figure 7) from diffuse-reflectance-mode optical spectra (Figure S7).

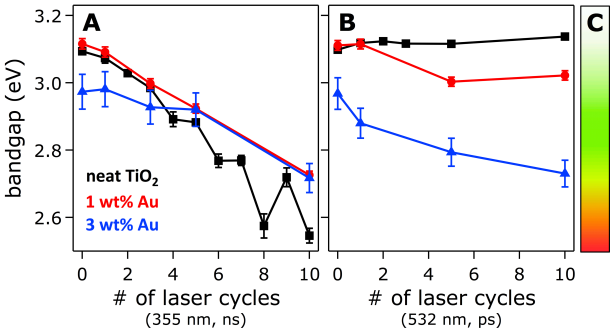

Figure 7: Bandgaps of neat TiO_2 particles (black squares), or with nominally 1 (red circles) or 3 wt% (blue triangles) gold nanoparticles, laser-irradiated by ns-355-nm (A) or ps-532-nm (B) pulses. Expected material color based on bandgap alone (C).

Upon irradiation by ns-355-nm pulses, we obtained a linear decrease of bandgaps from 3.1 to 2.6 eV (Figure 7 A), similar to observations by Chen et al.[23] We did not detect significant changes in the bandgap energies for neat TiO_2 that had been subjected to ps-532-nm pulses. Bandgaps became smaller for TiO_2–AuNP composites upon ps-532-nm irradiation, and the decrease was more pronounced with more gold. We obtained slightly lower bandgaps for TiO_2 with nominally 3 wt% AuNPs compared to neat TiO_2, even without laser processing, indicative of rutilization by AuNP physisorption, in line with observations by Strunk et al.[92] and Jovic et al.[52] We explain the observed decrease of TiO_2 bandgaps as a function of AuNP loading and ps-532-nm laser energy dose by electric field enhancements that are most pronounced near the interface between AuNP and TiO_2, similar to our ZnO results (conceptual details are illustrated in Figure 6).

The bandgap reductions we observed redshifted the light absorption of TiO_2 into the visible spectral range but, importantly, cannot explain the blue colors we detected upon laser processing (Figure 1). For clarity, we included in Figure 7 C a color gradient that displays what color any material would have if its appearance were solely due to bandgap absorption. In other words, the bar in Figure 7 C shows the complementary color of each color that corresponds to a certain bandgap energy. For example, our un-irradiated TiO_2 nanoparticles exhibited a bandgap of 3.1 eV, thus the material would appear almost white with a light green hue if its color were exclusively a result of its bandgap. Laser irradiation by ns-355-nm pulses decreased the bandgap to 2.6 eV, corresponding to absorption of blue light; hence, the material would look yellow-orange, like the color depicted in Figure 7 C for 2.6 eV, if its bandgap were the only source of color. But our materials turned deep blue upon laser irradiation. Ergo, the physical origin of color in laser-irradiated TiO_2 nanoparticles must be something other than bandgap.

Next, we assessed how the crystal phases of our P25 TiO_2 particles evolved upon laser irradiation and AuNP adsorption. We assigned the detected XRD patterns to a mixture of rutile (PDF 1-1292; ICDD, 2012) and anatase (PDF 21-1272; ICDD, 2012) TiO_2; no other crystal phases were present (Figures S8 – S13). We observed slight peak shifts of maximal ± 0.085° but could not detect trends as a function of irradiation energy dose. Therefore, we surmise that a Doppler effect due to vibrations during the measurement caused the shifts rather than changes of lattice parameters. Our initial P25 TiO_2 was a mixture of 80 % anatase and 20 % rutile,[93] complicating structural analysis compared to phase-pure

ZnO. We note that rutile is the thermodynamically more stable polymorph,[94] and anatase has been found to exhibit higher photocatalytic activity.[95]

We analyzed the rutile-to-anatase ratio as a function of laser irradiation, by integrating the anatase(101) peak and dividing the resulting area by the integrated rutile(110) reflection (Figure 8).

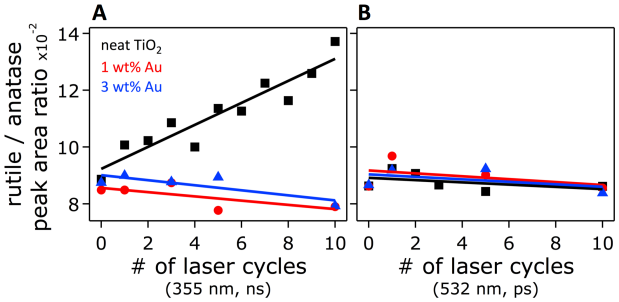

Figure 8: Relative rutile-to-anatase ratio after ns-355-nm (A) or ps-532-nm (B) irradiation, from XRD data. The lines are linear fits.

We found that the relative rutile-to-anatase ratio of neat TiO_2 increased linearly with increasing energy dose of ns-355-nm pulses, consistent with laser-induced high thermal loads, as the relative amount of the thermodynamically more stable rutile rose linearly. We attribute our finding of linearly decreased bandgap as a function of ns-355-nm irradiation (Figure 7 A) to this linear increase of the relative rutile-to-anatase ratio. In contrast, the relative rutile-to-anatase ratio did not significantly change upon irradiation by ps-532-nm pulses (Figure 8 B), consistent with low thermal loads due to the low absorptivity of TiO_2 at the longer wavelength, analogous to the situation with ZnO.

Interestingly, ns-355-nm irradiation of gold-modified TiO_2 nanoparticles led to a behavior opposite of that of neat TiO_2: the rutile-to-anatase ratio of TiO_2–AuNP composites decreased linearly with increasing energy dose, albeit with less than half the slope of that of neat TiO_2 (Figure 8 A). We hypothesize that the presence of AuNP suppressed rutile formation during ns-355-nm laser processing. Tang et al. recently showed that anatase had a significantly higher susceptibility for AuNP encapsulation than rutile.[96] Accordingly, the higher affinity of AuNP towards anatase suppressed the formation of rutile in our composite materials. We surmise that the additional rutile that had been generated upon laser irradiation of *neat* TiO_2 was located at the TiO_2 particle *surface*, as AuNP physisorption in composites most impacts surface structures. Highlighting the complex interactions of AuNPs on TiO_2, Strunk et al. reported rutilization of pure anatase surfaces after AuNP deposition.[92] Also at play may be a strain-driven mechanism that reaches deeper into TiO_2 nanoparticles and causes dislocations to migrate and restructure, consistent with results by Zhou et al., who reported migration and clustering of dislocations in AuCu nanoparticles as a function of temperature.[97] We note that the penetration depth of UV light in TiO_2 is ca. 125 nm, estimated as the inverse absorptivity, which is ca. 80,000 cm^{-1} at 3.5 eV,[98] and our P25 TiO_2 nanoparticles had sizes of ca. 25 – 50 nm.

We quantified the gold content of TiO_2–AuNP composites as a function of laser irradiation, analogous to our ZnO data. We found that faceting of AuNPs was unlikely because the Au(200)/Au(111) ratio remained virtually constant. We integrated the Au(200) reflection and normalized it to the sum of the peak areas of the anatase(101) and rutile(110) reflections, to obtain the relative amount of Au(200) per preparation, irrespective of the rutile-to-anatase ratio changes upon laser processing (Figure 9 and S10 – S13).

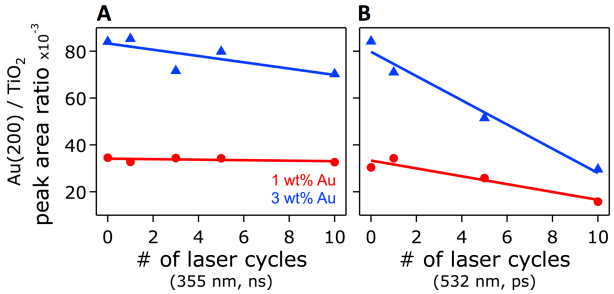

Figure 9: Relative Au(200)-to-TiO_2 ratios that indicate how much gold remained on the laser-treated TiO_2 nanoparticles. A, ns-355-nm pulses; B, ps-532-nm pulses. Gold percentages are nominal amounts; the lines are linear fits.

We found that ns-355-nm irradiation of TiO_2–AuNP composites led to a steady or slightly decreasing relative gold content for nominally 1 or 3 wt% Au, respectively (Figure 9 A). In contrast, we observed similar trends as with our ZnO materials with ps-532-nm pulses: Irrespective of the nominal AuNP loading, the amount of gold that remained on TiO_2 linearly decreased with increasing irradiation dose, more so for more gold (Figure 9 B). We explain the observed gold losses from TiO_2 nanoparticles upon laser irradiation by laser-induced, shock-wave-mediated surface cleaning, analogous to the discussion of our ZnO results.[57-59]

Overall, measured bandgap changes and XRD data cannot explain the observed colors of TiO_2 nanoparticles upon pulsed-laser irradiation (Figure 1), akin to the situation with ZnO. Therefore, we once more turned to PL experiments to quantify defects and identify their locations, i.e. within the TiO_2 bulk or at its surface.

The PL intensities of TiO_2 were much lower than those of ZnO. We applied a deconvolution process similar to that described above (see SI for more details). Serpone et al. reported seven PL transitions for TiO_2.[99] Significant uncertainty would arise from a fit with seven convoluted Gaussians; therefore, we limited the number of unknowns in our fit routine to four main defect families (Table 2), analogous to published work.[32, 100-102]

Table 2: Optically active defect families in TiO_2 and associated emission wavelengths and photon energies.

Origin of PL	Emission wavelength (nm)	Photon energy (eV)
Bandgap transition	390	3.18
Self trapped exciton (STE)	406	3.05
Shallow trap (ST#1)	456	2.72
Shallow trap (ST#2)	510	2.43

Reported defect-family energies varied. We took the bandgap PL to be centered at 390 nm, in keeping with a recent report by Kunti et al.[103]. According to Strunk et al., self trapped exciton (STE) and shallow trap (ST) contributions are located at 406 and 456 nm, respectively.[32, 102, 103] We detected an additional green emission

centered at 510 nm, which is close to values reported by Song and Gao.[104] As an example, 2D PL data and defect assignments of un-irradiated neat TiO_2 are shown in Figure 10. We denote shallow-trap emissions centered at 456 and 510 nm ST#1 and ST#2, respectively. The fits matched the 2D PL spectra well and allowed us to quantify contributions from bandgap states and individual defect types.

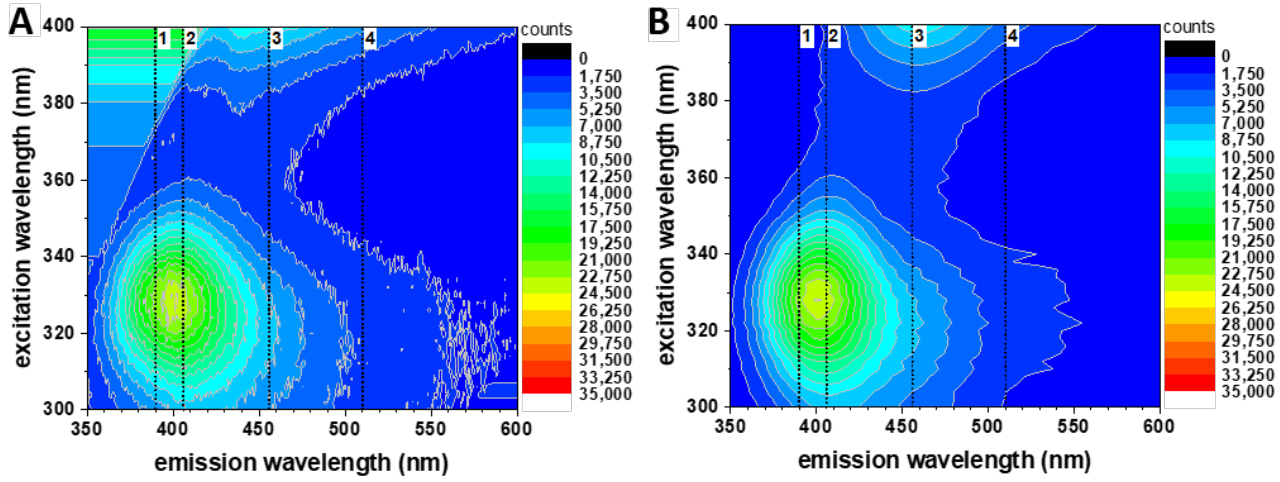

Figure 10: 2D PL data of un-irradiated neat TiO_2 particles (A) and simulated spectra (B); data analysis details are in the SI. The dotted lines indicate known optically active defects, as described in the text and Table 2.

Locations of TiO_2 defects (surface or bulk) have been inferred from relative defect emission intensities in TiO_2 whose surface was in contact with quenchers.[32, 100-102] The precise emission energies of individual defect sites, such as Ti or O interstitials or Ti or O vacancies, are unknown to date. But low-energy emissions, assigned to shallow traps, were reported to be sensitive to adsorbed species and, therefore, thought to be located near the TiO_2 surface.[32, 100-102] In contrast, higher-energy PL has been attributed to self-trapped excitons, which was insensitive to the environment around TiO_2, indicative of originating from deep within the TiO_2 bulk.[32, 101, 102] Contributions of bandgap states and different TiO_2 defects to the detected PL signal as a function of material preparation (laser type and irradiation energy dose) are depicted in Figure 11; all measured and deconvoluted 2D PL data and fits are shown in Figures S15 and S16.

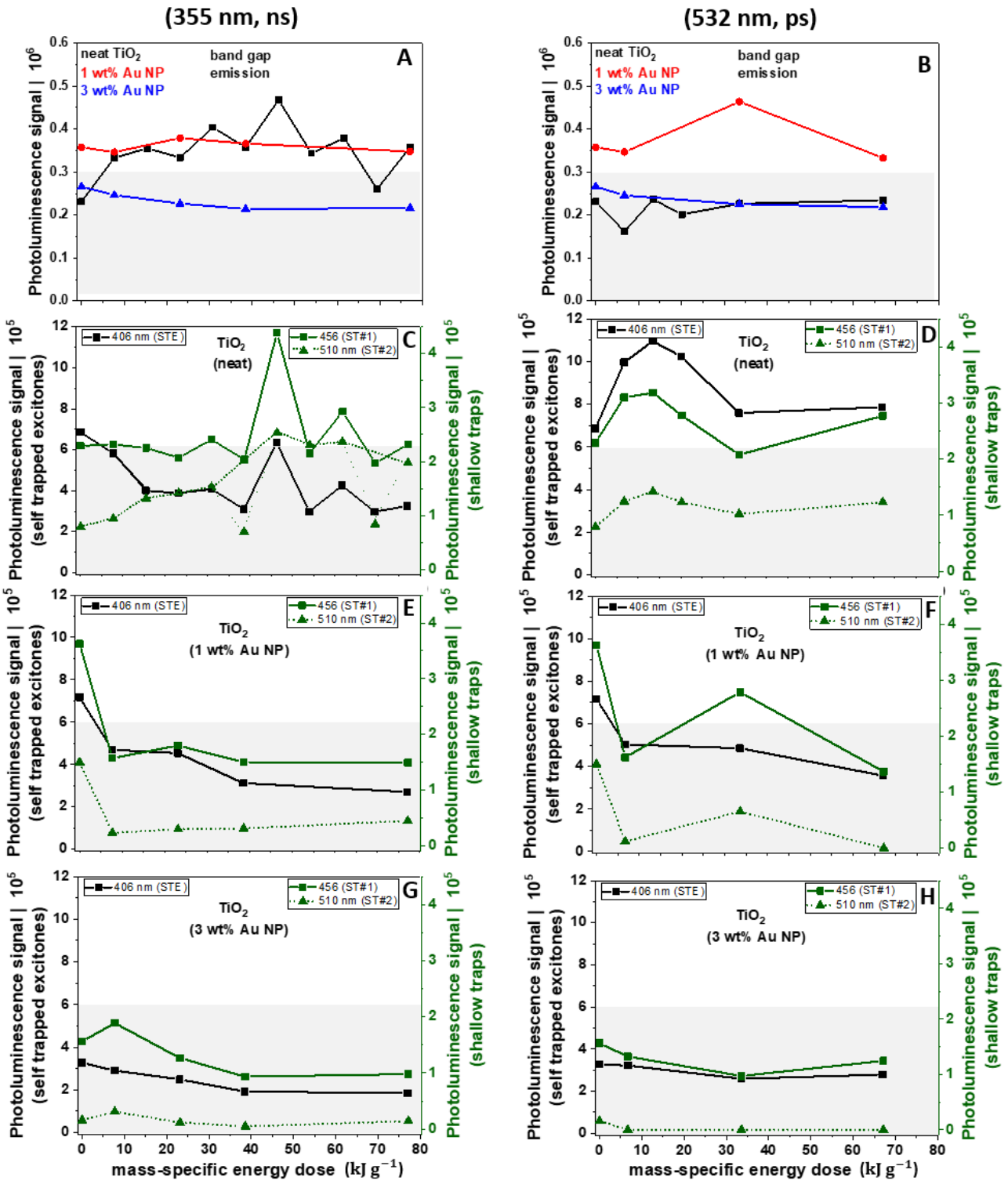

Figure 11: Contributions of bandgap states (A, B) and different TiO_2 defects to the measured PL signal as a function of irradiation parameters (laser type and irradiation energy dose). TiO_2 nanoparticles were irradiated by ns-355-nm (left) or ps-532-nm (right) pulses; neat TiO_2 (C, D), TiO_2 with nominally 1 (E, F) or 3 wt% (G, H) AuNPs. Lines are included to guide the eye. The gray background serves as a reference to aid visual comparisons of panels.

We found that pulsed-laser irradiation, irrespective of wavelength and pulse duration, did not significantly alter bandgap emissions (Figure 11 A, B). Gold functionalization affected bandgap and defect emissions of un-irradiated TiO_2 (0 kJ g^{-1}) in a similar way as in ZnO: We detected enhanced bandgap and near-surface ST emissions in TiO_2–AuNP composites with nominally 1 wt% Au, whereas TiO_2 with nominally 3 wt% Au exhibited decreased PL, presumably due to higher absorption of excitation and emitted light by AuNPs. We note that gold functionalization did not modify the bulk STE PL intensity.

Yet, pulsed-laser irradiation and, importantly, the type of laser light, to which the TiO_2 nanoparticles were exposed (Figure 11 C, D) very much affected defect emissions. Increasing energy doses of ns-355-nm pulses led to a steady increase of green color centers in neat TiO_2, attributable to near-surface shallow traps, ST#2, whereas the density of self-trapped excitons, STE, in the bulk decreased; shallow traps emitting at 456 nm, ST#1, remained largely constant (Figure 11 C). Gold-functionalized TiO_2 materials that were irradiated by ns-355-nm pulses showed markedly quenched PL from shallow traps (Figure 11 C, E, and G), both ST#1 and ST#2, whereas the STE signal remained largely unaffected, compared to neat TiO_2.

The PL intensities of ST#2 without and with AuNP functionalization are consistent with our XRD data of TiO_2: We observed steadily increasing surface rutilization as a function of ns-355-nm energy dose of neat TiO_2 particles (Figure 8 A). Rutile was generated during laser processing under high thermal load conditions (up to 77 kJ g^{-1}) because of the large absorption cross-section of TiO_2 in the UV spectral range.[98] We concluded from our XRD results that rutilization occurred mainly at the TiO_2 nanoparticle surface (Figure 12) and was suppressed when AuNPs were present during laser treatment.

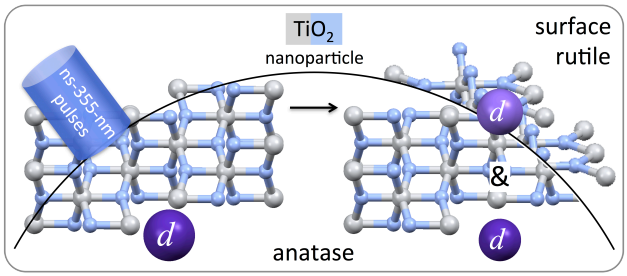

Figure 12: Schematic of surface rutilization of TiO_2 nanoparticles upon ns-355-nm irradiation. The structures are based on crystal structures of anatase[105] and rutile[106] TiO_2. Defects (*d*) are illustrated by purple spheres, whose sizes are indicative of observed defect densities; dark purple, bulk defects, light purple, surface defects.

The ST#2 PL was significantly lower in TiO_2–AuNP composites, both for nominally 1 and 3 wt% Au (Figure 11 E, G), compared to neat TiO_2. This PL quenching is consistent with our detection of more anatase upon ns-355-nm irradiation of TiO_2–AuNP composites in our XRD data. And we delineated above that AuNPs were capable of quenching *surface* defect PL in ZnO materials due to damping of dipole oscillations;[63] note that in case of ZnO, ns-355-nm light generated mainly bulk defects and almost no surface defects, most likely due to the absence of a phase transition in ZnO.

Oxygen vacancies are typical defects in TiO_2 and have extensively been studied,[7] mainly by DFT calculations.[107-110] Oxygen vacancies were found to be most stable on the surface of rutile structures, whereas in anatase oxygen vacancies exhibited lower energy states in subsurface layers.[107-110] EPR studies on surfaces of hydrated P25 TiO_2 in the presence of adsorbed oxygen revealed that several oxygen and hydroxide species formed upon UV-irradiation; oxygen anion, O^-, superoxide, O_2^-, hydroxide radicals, and oxygen vacancies, manifesting as Ti^{3+}, were identified.[111] Perturbation of a regular Ti^{4+} site by trapping of a photoelectron from the conduction band after UV irradiation at low temperature to form a Ti^{3+} center and capture of holes in the form of reactive oxygen species have been thoroughly investigated by EPR methods.[112, 113] These Ti^{3+} centers turn titania blue and have been reported to enhance photocatalytic activity.[114-116]

Accordingly, we attribute the blue coloration of our ns-355-nm irradiated TiO_2 materials to the formation of Ti^{3+} defects, consistent with our observations of (1) bandgap reduction as a function of ns-355-nm energy dose, (2) surface rutilization of neat TiO_2 nanoparticles derived from XRD data (Figure 8 A), and (3) increased ST#2 emission in our PL data (Figure 11 C). We found that our laser processing generated stable Ti^{3+} defects, as we could not detect any decolorization upon heating to 450 K in nitrogen or oxygen atmosphere.

In ns-355-nm-irradiated TiO_2–AuNP composites, we observed shrinking bandgaps (Figure 7 A), a slightly decreasing rutile-to-anatase ratio (Figure 8 A), and decreasing ST#2 defect emissions (Figure 11 E and G). The experimentally determined bandgap energy of TiO_2 anatase is higher (3.2 eV)[117-118] than that of rutile (3.0 eV).[117,119,120] Our observation of a decreasing bandgap without rutilization in TiO_2–AuNP composites upon ns-355-nm irradiation indicates that defects created in-gap states that reduced the bandgap.

As mentioned above, Tang et al. reported that the strong metal–support interaction of gold on titania, mediated by electron transfer from the reducible oxide TiO_2 to AuNPs and gold encapsulation by a TiO_x overlayer, markedly improved the redox stability of TiO_2–AuNP composites; anatase was most susceptible to encapsulation.[96] Accordingly, we surmise that AuNPs stabilized surface defects in anatase during ns-355-nm-laser treatment, thus preventing the rutilization we observed in neat TiO_2. The ST#2 PL of TiO_2–AuNP composites originated initially from UV-light-induced bulk and surface defects, analogous to those in neat TiO_2. These defects were stabilized by the close proximity of the AuNPs, in agreement with work by Strunk et al.;[92] activation of oxygen to peroxo species has also been reported at Au–TiO_2 materials and was applied to selective oxidation reactions.[121] We note that strong dipole damping by AuNPs quenched surface ST#2 PL (Figure 6 B). Enhanced absorption of excitation and emitted light by AuNPs may also contribute to lower detected PL intensities.

We obtained very different results upon ps-532-nm irradiation of TiO_2 (Figure 11 D, F, and H): PL intensities of all defect types in neat TiO_2 first rose and then returned to initial values as a function of applied energy dose (Figure 11 D). Our data at lower energy doses (0 – 20 kJ g^{-1}) suggest formation of additional luminescent STE and ST sites during the first laser pulses. At higher energy doses (≤ 80 kJ g^{-1}), we observed curing of these defects (Figure 13), in agreement with reports by Yang et al. and Kernazhitsky et al., who described lower PL after calcination of TiO_2 and concomitant decrease of surface area or hydration.[32, 122]

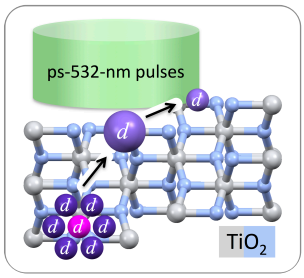

Figure 13: Schematic of defect healing at TiO_2 nanoparticle surfaces upon ps-532-nm irradiation. The structure is based on the crystal structure of anatase TiO_2.[105] Defects (d) are illustrated by purple spheres, whose sizes are indicative of observed defect densities; magenta, preexisting defect, dark purple, laser-generated bulk defects, light purple, surface defects.

We presume that mainly in-gap states from preexisting TiO_2 defect sites contributed to the absorption of ps-532-nm pulses, similar to our ZnO results.[86] We did not detect significant changes of the bandgaps (Figure 7 B) or the relative rutile-to-anatase ratio (Figure 10 B) of neat TiO_2 irradiated by ps-532-nm pulses. Positron-annihilation experiments by Yan et al. demonstrated increased defect densities at TiO_2 surfaces after calcination, indicative of migration of sub-surface intra-grain monovacancies towards grain boundaries.[32] Accordingly, we attribute the stronger PL signal (Figure 10 D) to the formation of more defects in the vicinity of preexisting defects. In other words, our ps-532-nm pulses induced new defects close to initially present defective sites, and these new defects ultimately diffused towards the surface during further laser irradiation. We found that above 20 kJ g^{-1}, laser-induced defects reached the TiO_2 surface and most likely reacted with water[110, 123, 124] that surrounded the nanoparticles during laser processing; this way, defects were cured. This defect healing led to a net attenuation of detected defect PL at high laser energy dose (Figure 11 D).

TiO_2–AuNP composites with nominally 1 or 3 wt% AuNPs exhibited quenched PL of all defect types (Figure 11 F and H) upon ps-532-nm laser processing. Presumably, near-field enhancement by AuNPs increased defect formation close to the TiO_2–AuNP interface, evidenced by the shrinking bandgap as a function of ps-532-nm-laser energy dose (Figure 7 B). Our spherical TiO_2 nanoparticles had diameters of ca. 25 – 50 nm; therefore, the maximum distance of a defect to the TiO_2–AuNP interface was ca. 12.5 – 12 nm, well within the range of dipole damping by AuNPs (Figure 6). As a result, we observed low PL intensity.

Summary of Defect Generation in Laser-Processed ZnO and TiO_2 Materials

A schematic illustrating defect generation mechanisms upon ns-355-nm or ps-532-nm irradiation of neat ZnO or TiO_2 is shown in Figure 14.

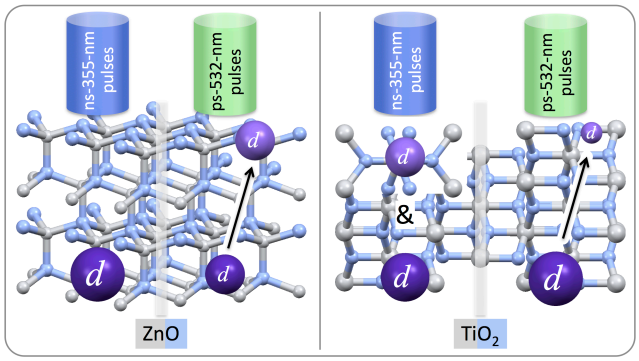

Figure 14: Schematic of the type of defect generation upon laser irradiation of ZnO or TiO_2 nanoparticles. The structures are based on crystal structures of wurtzite ZnO,[125] anatase TiO_2,[105] and rutile TiO_2.[106] Defects (d) are illustrated by purple spheres, whose sizes are indicative of observed defect densities; dark purple, bulk defects, light purple, surface defects.

Laser processing of neat and gold-nanoparticle-functionalized ZnO and TiO_2 nanoparticles by ns-355-nm or ps-532-nm light created defects in the nanomaterials, as summarized in Table 3.

Table 3: Summary of defect generation by laser processing.

Nanomaterial	Increasing energy doses of ns-355-nm pulses	Increasing energy doses of ps-532-nm pulses
ZnO, neat	**Bulk** defects, $V_{Zn}(I)$ Zn vacancy defects ↑	Small changes because of small absorption cross section, preexisting Zn vacancy defects absorbed the laser light **Bulk** defects ↓, **surface** defects ↑ by defect diffusion
ZnO–AuNP composites	**Bulk** defects, $V_{Zn}(I)$ Zn vacancy defects ↑ High energy dose: Zn vacancy defects ↓ by isochoric-melting-assisted diffusion	**Surface** defects ↓ due to dipole damping by AuNPs
TiO_2, neat	Surface rutilization, formation of many defects, e.g. Ti^{3+} **Surface** ST#2 defects ↑, **bulk** STE defects ↓	Generation of new defects close to preexisting defects **Surface** and **bulk** defects ↑, then ↓ by diffusion of bulk defects to the surface and laser-induced reaction with surrounding water, resulting in **defect healing**
TiO_2–AuNP composites	Steady rutile-to-anatase ratio **Surface** defects ↓, **bulk** defects steady	**Surface** defects ↓ by dipole damping

Overall, our laser processing induced bulk and surface defects in TiO_2 nanoparticles, and we derived the following mechanisms from optical spectra, XRD, and PL data: Irradiation by ns-355-nm pulses induced bandgap contraction and surface rutilization, due to the high absorptivity of TiO_2 at 355 nm and the long laser pulse duration (compared to the timescale of electron-phonon relaxation

dynamics). Oxygen vacancies and reactive oxygen species formed during structural rearrangements to rutile, and near-surface shallow traps were enhanced (strong green PL). The presence of AuNPs during ns-355-nm laser processing suppressed rutile formation; newly formed defects that were stabilized by nearby AuNPs led to smaller bandgaps. Due to the small size of our TiO_2 nanoparticles, all defects were close enough to adsorbed AuNPs to experience dipole damping, and the PL of all defect types was quenched.

In contrast, irradiation of neat TiO_2 nanoparticles by ps-532-nm pulses did not cause structural rearrangements or bandgap changes, due to the low absorptivity of TiO_2 for 532-nm light. Absorption of 532-nm pulses occurred at preexisting TiO_2 defects, and new defects appeared near those preexisting defects (increased PL as a function of applied ps-532-nm energy dose). At highest energy doses, defect diffusion to and healing at the TiO_2 surface occurred (weaker PL). Presence of AuNPs during ps-532-nm laser processing lowered the PL intensities of all defect types and led to linearly shrinking bandgaps as a function of energy dose, more so with more gold. We assigned these defects to surface locations.

We note that our results for TiO_2 and ZnO are not directly comparable, as the materials had very different sizes and morphologies; our TiO_2 nanoparticles were ca. 25 – 50 nm spheres, and the ZnO consisted of ca. 250 nm × 125 nm rods. In the much smaller TiO_2 nanoparticles, defects were always in much closer proximity to the surface. Because of these short defect diffusion distances in our TiO_2 nanoparticles and the surface rutilization upon ns-355-nm laser irradiation, defects were created within the bulk and at the surface of TiO_2. In contrast, the same laser conditions generated only bulk defects in the larger ZnO nanorods. Irradiation by ps-532-nm pulses resulted in surface defects in both transition metal oxides (Figure 14).

Correlation of Surface and Bulk Defects in ZnO and TiO_2 Nanoparticles to Photoelectrochemical Performance

We collected photoelectrochemical (PEC) data, as we wanted to understand how laser-induced bulk and surface defects affected photocurrent generation in neutral aqueous electrolytes without or with sulfite as sacrificial hole acceptor under simulated 1 sun, AM1.5G illumination and anodic polarization. We quantified photocurrent densities at 0.7 V vs the reversible hydrogen electrode, RHE, as photocurrents exhibited a plateau at this applied potential. Photocurrents as a function of ZnO or TiO_2 material preparation are shown in Figure 15; corresponding linear sweep voltammograms are shown in Figures S17 – S20. Dark currents were flat at moderate potentials and did not differ much between materials. We note that we assessed thin TiO_2 and ZnO films and used front-side illumination. We did not chase record PEC performances but wanted to observe relative trends as a function of laser processing and AuNP functionalization.

We found that PEC performance decreased for almost all ZnO material preparations as a function of pulsed-laser irradiation, regardless of laser parameters, or presence of AuNPs or sulfite. Only one ZnO material (neat ZnO, irradiated by 7.7 kJ g^{-1}, ps-532-nm pulses, 1 cycle) showed slightly increased photocurrent generation in the presence of sulfite.

Interestingly, photocurrent densities did not differ much in electrolytes with or without sacrificial hole acceptor (Figure 15 A – D). Typically, photocurrents are much larger in aqueous electrolytes with a sacrificial hole acceptor; the hole-acceptor oxidation reaction is much faster than water oxidation, leading to more efficient depletion of photogenerated holes at the photoanode–electrolyte interface and thus higher currents.[126, 127] Our observation of near-constant photocurrents with or without sulfite suggests that the kinetics of holes reacting at the ZnO–electrolyte interface were not limiting photocurrent generation, but that most photogenerated holes were lost before they reached the electrolyte. In the following, we call this scenario the "carrier transport limitation regime".

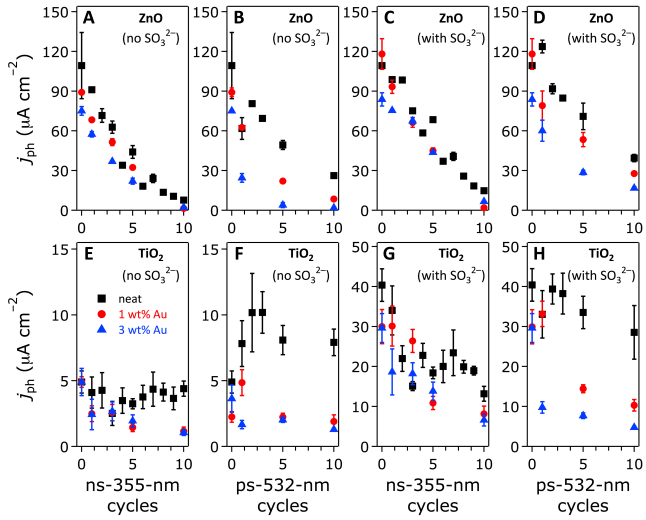

Figure 15: Photocurrents j_{ph} at 0.7 V vs. RHE of neat ZnO or TiO_2 particles (black squares), and with pre-irradiation-adsorbed nominally 1 (red circles) or 3 wt% (blue triangles) AuNPs. The materials were subjected to up to 10 cycles of ns-355-nm (A, C, E, and G) or ps-532-nm (B, D, F, and H) laser pulses. Electrolytes were 0.1 M aqueous pH 7.0 sodium phosphate buffer (no SO_3^{2-}; A, B, E, and F) or 0.1 M aqueous pH 7.0 sodium phosphate buffer with 0.5 M Na_2SO_3 as sacrificial hole acceptor (with SO_3^{2-}; C, D, G, and H).

Long diffusion distances from bulk defect sites to the ZnO surface existed in ZnO nanoparticles because they had a size of ca. 250 nm × 125 nm. Since the photocurrent densities were very similar in electrolytes with or without sacrificial hole acceptor, we surmise that even in electrolytes without sulfite the reaction of holes at the ZnO surface outpaced carrier transport, i.e. the carrier transport limitation regime was operational. Photocorrosion of ZnO in aqueous electrolyte may also be at play.

Physisorption of AuNPs after irradiation of ZnO reduced photocurrents in most cases. Addition of nominally 3 wt% Au had a greater effect than 1 wt% Au, and the decrease was much more pronounced with ps-532-nm pulses, which induced mainly near-surface defect density, than with ns-355-nm irradiation, which primarily produced bulk defects. In fact, ZnO–Au composites that were irradiated by ns-355-nm pulses performed about as well as neat ZnO in electrolytes with sulfite (Figure 15 C), and photocurrents of ZnO–Au composites were only slightly lower than those of neat ZnO in aqueous buffer without sulfite (Figure 15 A).

We explain these observations by considering our findings on how pulsed-laser irradiation affected structure and defect formation. PL was lowest for ZnO–Au composites with nominally 3 wt% AuNPs that were exposed to ps-532-nm pulses; defects were mostly located near the ZnO surface, and AuNPs preferentially quenched dipole oscillation and exciton generation. Hence, the number of excitons near the surface was lowered. AuNPs at the ZnO surface also absorbed incident simulated sunlight and detrimentally affected PEC performance. As a result, we found a strong

attenuation of photocurrent production of AuNP–ZnO composites, regardless of the presence or absence of sulfite (Figure 15 B and D).

In contrast, ns-355-nm pulses interacted with aqueous suspensions of ZnO particles such that high bulk defect densities emerged; the nanosecond pulse duration and large absorption cross section of ZnO for 355 nm induced high thermal loads and caused isochoric melting of ZnO. As defect–AuNP interactions must necessarily occur near or at the ZnO surface, and since we obtained only minimally different photocurrents of ZnO irradiated by ns-355-nm pulses as a function of adsorbed AuNPs (0, nominally 1, or 3 wt%, Figure 15 A and C), we conclude that the low photocurrents resulted from defects that were predominantly located in the ZnO bulk. Note that ZnO had rod shape and was up to 10 times larger than the sphere-shaped TiO_2 nanoparticles, giving rise to long hole transport distances through ZnO. As a result, photocurrents were limited by bulk-to-electrolyte-interface hole transport, independent of the presence or absence of hole acceptor. As the bulk defects and AuNPs were spatially separated, AuNP loading played only a minor role for photocurrent generation. More physisorbed gold attenuated photocurrents slightly more, presumably due to parasitic light absorption (Figure 15 A and C).

For TiO_2, we observed at least four times higher photocurrents in electrolytes with sacrificial hole acceptor (Figure 15 E and F), compared to sulfite-free conditions (Figure 15 G and H). PEC performance decreased steadily for ns-355-nm-irradiated TiO_2, whereas ps-532-nm irradiation of TiO_2 yielded markedly higher photocurrents in sulfite-free electrolytes as a function applied energy dose; in sulfite-containing electrolytes, the measured photocurrents were fairly stable.

We explain our observations by taking into account how the kinetics of different chemical reactions (i.e. with or without hole-accepting sulfite) at the TiO_2–electrolyte interface affected surface defects and how bulk defects impacted hole transport within TiO_2. Depending on electrolyte conditions, we propose two different rate-limiting steps: With sulfite, the reaction of holes at the TiO_2 surface was very fast, and only hole transport characteristics, such as hole mobility, trapping, and diffusion distances, within the TiO_2 bulk limited PEC performance. Ergo, the steadily decreasing photocurrents of laser-treated TiO_2 in the presence of sulfite (Figure 15 G and H) were likely caused by less efficient hole transport, e.g. due to increased material strain; the carrier transport limitation regime was operational.

We obtained higher photocurrents in TiO_2 nanoparticles that had been irradiated by ps-532-nm pulses (Figure 15 H), compared to those of ns-355-nm-treated TiO_2 (Figure 15 G); we explain this finding by the rutile-to-anatase ratio we established by analysis of XRD data. Anatase is photocatalytically more active than the thermodynamically more stable rutile polymorph.[94] Our ns-355-nm pulses caused surface rutilization (Figure 8) and concomitant formation of a photoelectrochemically less active layer. In the carrier transport limitation regime, where surface defects play a minor role, it was this polymorph activity difference that governed PEC performance. In contrast, TiO_2 nanoparticles that had been subjected to ps-532-nm pulses contained higher amounts of more active anatase and thus exhibited higher photocurrents and a less steep decrease as a function of irradiation dose (Figure 15 G and H).

Without sulfite in the electrolyte, PEC performance appeared rate limited by slow oxidation kinetics; hole transport through the solid was faster, particularly through the ca. 25 – 50 nm TiO_2 spheres, whose small size led to short maximum diffusion distances; note that in case of the much larger ZnO nanoparticles, bulk defects instead of oxidation kinetics limited photocurrent generation. In case of the smaller, ns-355-nm-irradiated TiO_2 nanoparticles, the number of luminescent surface defects determined PEC performance, which we denote the "surface defect limitation regime".

We obtained similar trends in our PL (Figure 11 C, E, G and D, F, H) and PEC (Figure 15 E and F) data for TiO_2 in sulfite-free electrolytes. According to our proposed mechanism, defect densities, assessed by PL analysis, rather than hole mobilities, primarily controlled photocurrent generation, for both laser processing conditions (Figure 15 G and H).

Defect formation in TiO_2 upon laser irradiation by ns-355-nm pulses was different from our ZnO results, presumably because of the TiO_2 nanoparticle size of ca. 25 – 50 nm, which allowed the UV light to completely penetrate the TiO_2: increasing energy doses of ns-355-nm pulses primarily induced near-surface shallow traps (ST#2) at the expense of bulk self-trapped excitons (STE) in neat TiO_2. In line with our arguments above, we explain the observed decrease of PEC performance as a loss of photogenerated holes at surface ST#2 defects, compounded by rutilization. The presence of AuNPs during laser treatment markedly quenched PL from shallow traps but did not modify the defects themselves; photocurrents remained low (Figure 15 E and G).

With ps-532-nm irradiation, PL intensities of bulk and surface defects in neat TiO_2 as a function of applied energy dose first rose and then returned to initial values, as a result of *defect healing* at high laser energies (Figure 15 D and F). Photocurrent generation in sulfite-free electrolytes significantly increased first and then plateaued at 33.5 kJ g^{-1} (5 cycles). We note that we obtained lower ST#2 defect densities with ps-532-nm than with ns-355-nm irradiation, in line with our observation of higher photocurrents in TiO_2 after exposure to green compared to UV laser light. Photocurrent generation in sulfite-containing electrolytes remained almost constant, with a slight downward trend at energy doses above 23.1 kJ g^{-1} (3 cycles).

Our TiO_2–AuNP composites exhibited lowered photocurrents in most cases for all irradiation conditions; more gold had more effect. As in case of ZnO, ns-355-nm-irradiated TiO_2–Au composites performed in electrolytes with sulfite (Figure 15 G) similarly well as neat TiO_2, and photocurrents of TiO_2–Au composites were only slightly lower than those of neat TiO_2 in aqueous buffer without sulfite (Figure 15 E). TiO_2–AuNP composites that were irradiated by ps-532-nm pulses exhibited low or rapidly decreasing PEC performance, more so with more gold, in electrolytes without or with sulfite, respectively. We found more bulk STE and surface ST#1 defect emission in TiO_2–AuNP composites that were irradiated by ps-532-nm pulses than those exposed to ns-355-nm light. As described above, presence of AuNPs strongly quenched PL, exciton formation, and in turn photocurrent generation by dipole damping.[63]

Our results demonstrate that we were able to more than double photocurrent production of neat TiO_2 nanoparticles by ps-532-nm laser processing. Detailed structural, bandgap, and defect type analyses allowed us to explain this photocurrent generation improvement by defect healing upon laser irradiation. We established

the mechanisms by which laser processing generated surface and bulk defects in ZnO and TiO_2 photoanodes and shed light on the key role these defects play for PEC performance.

Conclusions

Laser processing of neat ZnO and TiO_2 nanoparticles and ZnO or TiO_2–AuNP composites by ns-355-nm or ps-532-nm pulses created surface and bulk defects in the nanomaterials that directly correlated with photocurrent production. We obtained more than two-fold enhanced PEC performance of TiO_2 nanoparticles upon irradiation by ps-532-nm pulses.

Laser irradiation and gold functionalization of ZnO and TiO_2 materials changed their absorption characteristics as a result of defect formation, not bandgap or crystal structure changes. Two-dimensional photoluminescence data allowed us to differentiate and quantify surface and bulk defects. Depending on laser parameters, we developed two defect formation mechanisms.

Irradiation by ns-355-nm pulses induced high thermal loads in ZnO and TiO_2 and generated mainly bulk defects due to isochoric melting, regardless of the absence or presence of AuNPs. In neat TiO_2, we observed rutilization, which was accompanied by the formation of surface defects in addition to bulk defects. The presence of AuNPs during laser processing prevented this phase transition, consistent with a stronger metal–support interaction between AuNPs and anatase than rutile, in agreement with reported work.[96] The PEC performance of neat and AuNP-functionalized ZnO and TiO_2 photoanodes decreased as a function of increasing ns-355-nm energy dose. Laser-generated bulk defects served as sites for detrimental carrier recombination in ZnO materials and photogenerated carriers were lost before they reached the photoanode–electrolyte interface, as evidenced by similar photocurrents with and without hole acceptor in the electrolyte. PEC performance was low in ns-355-nm-irradiated TiO_2 materials because of a combination of bulk and surface defects.

Laser processing by ps-532-nm pulses led predominantly to the formation of surface defects. The ps-532-nm light had a photon energy below the bandgaps of all materials and was mainly absorbed by preexisting defects that gave rise to in-gap states. We did not observe significant defect density changes in neat ZnO. But in TiO_2 we obtained first higher, then lower defect densities as a function of ps-532-nm energy dose. We explain this trend by formation of new defects at preexisting sites, followed by diffusion of bulk defects to the surface and laser-induced reaction with surrounding water that resulted in *defect healing*. We observed more than two-fold enhanced photocurrent generation upon this defect healing. We detected gold loss in ps-532-nm-irradiated ZnO and TiO_2–AuNP composites, more so with higher AuNP loading and energy doses, attributable to AuNP detachment due to the high absorption cross section of AuNPs for green light. Laser processing of ZnO and TiO_2–AuNP composites by ps-532-nm pulses led to increased surface defect densities, which we rationalized by AuNP-mediated defect formation due to near-field enhancement effects. High surface defect densities correlated with low photocurrents.

Overall, our data provide key insights about (1) the defect types and mechanisms that laser processing generated in ZnO and TiO_2 photoanodes, (2) the critically important yet often unacknowledged role that defects play for PEC performance, and (3) how controlled laser-induced healing of defects may be useful in the design of optimized solar fuels materials.

Materials and Methods

Laser processing, preparation of gold nanoparticles and physisorption on TiO_2 or ZnO nanoparticles was conducted at the University of Duisburg-Essen in the Faculty of Chemistry, Department for Technical Chemistry I. PL and diffuse reflectance experiments were carried out at the Center for Nanointegration Duisburg-Essen (University of Duisburg-Essen). Electrode preparation and photoelectrochemical measurements were performed at the Molecular Materials Research Center of the Beckman Institute at the California Institute of Technology. X-ray diffraction data were collected at the California Institute of Technology. All chemicals were used as received. Deionized water was obtained from MilliQ or Barnstead Diamond Nanopure systems and had a resistivity of ≥16 MΩ cm. Data analysis, unless otherwise noted, and graphing were performed with Igor Pro 6.37 (WaveMetrics, Inc.), Matlab R2017b, or OriginPro 2015G.

Laser irradiation of TiO_2 and ZnO particles. We started with commercially available titanium dioxide (TiO_2, P25 Aeroxide Evonik, ca. 25 – 50 nm spheres) or zinc oxide (ZnO, Sigma Aldrich, ca. 250 nm × 125 nm rods) powders; sizes were determined by electron microscopies (Figure S21). We processed 500 mg powder for each of the 70 samples (photos of dried laser-modified materials are shown in Figure 1). We laser-irradiated 500 mL of the aqueous particle dispersions (1 g L^{-1}) in a homebuilt liquid-jet flow reactor (Figure S1), which is described in detail in refs. 10, 11, 27, 128, 129. For conditions of high thermal load and isochoric melting, we employed a diode-pumped solid-state laser system (AVIA, Coherent Inc.) that operated at 85 kHz with 40 ns pulse length and emitted 355-nm pulses at a power of 19.4 W (denoted as ns-355-nm laser). For conditions of low thermal load and surface modification, we used 532-nm 10-ps pulses provided by an Ekspla picosecond Nd:YAG laser (Atlantic series) that emitted 7.5 W at the second harmonic (denoted as ps-532-nm laser). A Coherent Field MaxII-TOP power meter was used to measure average laser powers.

We stored 500 mL of particle suspension for up to 5 days until all particles had precipitated by ambient gravity to obtain powders; 400 mL of the clear supernatant was removed and the particles were re-dispersed by shaking, filled into 50 mL Falcon tubes, and centrifuged for 10 minutes at 4000 rpm in a Hettich Universal 32R centrifuge at 2701 RCF. The clear supernatant was decanted and the wet pellets were stored for 12 hours in an oven at 50 °C to gradually dry the laser-processed particles. We also determined the retrieval rate of the materials after this processing (Figure S22), as this rate is of interest from a materials processing point of view.

Physisorption of gold nanoparticles on ZnO and TiO_2 nanoparticles. We prepared ZnO or TiO_2–AuNP composites by physisorption of nominally 1 or 3 wt% laser-generated gold nanoparticles (wt% with respect to the mass of TiO_2 or ZnO) on the metal oxides before laser irradiation by ns-355-nm or ps-532-nm laser pulses. We fabricated colloidal gold nanoparticles by laser ablation of a gold target (Allgemeine 99.5% purity) immersed in 100 mL water, using the fundamental wavelength of an Nd:YAG picosecond laser (Ekspla, Atlantic Series, 10 ps, 100 kHz, 13.5 W). The gold colloids were produced by batch-wise ablation for 1 h in 100 mL, resulting in ca. 0.5 g L^{-1} gold. We added 25.0 or 8.3 g L^{-1} TiO_2 or 25.0 or 8.3 g L^{-1} ZnO to 500 mL of the gold colloid to obtain nominal gold mass loadings of nominally ca. 1 or 3 wt%, respectively.

Electron microscopy imaging. Scanning electron microscopy (SEM) images were collected with a FEI Quanta 400 instrument. We immobilized ZnO powder on a carbon adhesive pad mounted on a SEM sample holder. For transmission electron microscopy (TEM) imaging of P25 TiO_2 nanoparticles, we placed a droplet of a sonicated TiO_2 dispersion (0.1 g/L) on a carbon coated copper grid and let it dry in ambient conditions. We collected TEM images using a Philips EM400 instrument with an acceleration voltage of 120 kV.

Optical bandgaps. We determined optical bandgaps from diffuse powder reflection data, which we acquired using a Varian Cary spectrometer, equipped with a Spectralon reference (PTFE). We used the Kubelka-Munk formula to calculate absorptions. The bandgaps were determined by extrapolation of the absorption regime with linear increase. We took measurements in triplicates to obtain standard deviations for all un-irradiated and ns-355-nm-irradiated ZnO and TiO_2 nanoparticles.

X-ray diffraction (XRD) data. We used a Bruker D2 PHASER diffractometer with Cu Kα radiation (1.5418 Å; tube power 30 kV, 10 mA) to obtain XRD patterns. The instrument was equipped with 0.1° divergence, 2.5° Soller, and 0.6 mm detector slits. Additionally, a 3-mm secondary anti-scatter screen and a Lynxeye detector were applied. We used a resolution of 0.02° in 2θ and a counting time of 1 s per step, resulting in a data acquisition time of 54 min per sample. We mounted ~20 mg of each sample with Vaseline (X-Alliance GmbH) on a zero-diffraction silicon plate (MTI Corporation). Background subtraction, and XRD pattern matching was carried out using the Bruker DIFFRAC.SUITE software coupled to the International Centre for Diffraction Data powder diffraction file database (ICDD, PDF-2 Release 2012).

Photoluminescence (PL) data. We recorded PL spectra using a HORIBA Fluorolog 3 spectrometer equipped with a solid sample holder. The sample was placed in the focus of the collimated excitation light, titled at a 30° angle. According to the specification by HORIBA, a minimal amount of scattered light will reach the detector at this angle, which we verified experimentally. We covered the sample holder by alumina foil to prevent PL signals from the sample-holder coating that had been detected in preliminary tests. Before measurements, each sample was ground by a pestle in a mortar to homogenize the dried powders. About 20 mg of the ground powder was poured onto the sample holder, evenly dispersed and covered by a quartz lid, to form a uniform powder layer of about 1 mm thickness. After each measurement, the lid was extensively cleaned to avoid PL signals stemming from dust or residual fibers from cleaning cloths. We note that the cleaning process is of utmost importance, especially with materials like TiO_2 that have only weak PL. We used the spectral ranges and settings given in Table 4.

The ZnO PL signal was very distinct and broad, therefore we reduced the excitation bandpass, and thus increased accuracy and simultaneously limited the count rate (to about 10^5 counts per second) to prevent detector saturation. In case of TiO_2, we obtained only weak PL, therefore we used a larger bandpass to increase the count rate at the detector (to about 10^3 – 10^4). The integration time was set to 0.05 or 0.01 s for ZnO or TiO_2, respectively, in accordance with values recommended by the spectrometer manufacturer. In all TiO_2 spectra, an extra signal was visible in addition to the weak TiO_2 photoluminescence. We used non-luminescent silver powder (1 μm) as a control to identify the source of this unexpected peak and found it was a biasing signal caused by internal scattering of excitation light. The contribution of this scattering signal was reproducible and constant for all measurements; as a result, it did not affect relative changes in PL signals.

Table 4: Parameters for photoluminescence experiments.

Parameter	ZnO	TiO_2
Excitation range (nm)	290 – 390	300 – 400
Excitation increment (nm)	2	2
Excitation Bandpass (nm)	2	5
Emission range (nm)	350 – 700	350 – 600
Emission increment (nm)	1	1
Emission Bandpass (nm)	2	2

We recorded emission spectra as a function of excitation wavelength and baseline-corrected them. We determined the contributions of different defect centers (bulk or surface) to the overall spectrum by peak deconvolution, assuming Gaussian peak shapes. More details regarding analysis and deconvolution procedures are described in the SI.

Photoanode preparation. All photoelectrodes were prepared following a protocol established by Sinclair et al.[127] Briefly, 2 mm thick FTO-coated glass slices were cut into 0.9 cm × 2.4 cm pieces, treated for 10 min each in an ultra-sonication bath first in water, then in a 1:1 mixture of methanol and acetone (both EMD, HPLC grade). The bare FTO-glass pieces were dried in ambient air, briefly dipped in concentrated hydrochloric acid (Macron), and rinsed with copious amounts of water. After these cleaning steps, each FTO-glass piece was fitted with a circular working electrode area of 0.159 cm^2 and a contact for the wire lead by masking two FTO areas with 4.5-mm diameter disks and coating all remaining bare FTO with a black high-temperature spray paint (McMaster-Carr). A silver-coated copper wire was attached with silver paint (SPI, high purity) to the bare FTO at one short edge of the FTO-glass piece, and a glass tube surrounding the wire lead was glued to the FTO glass with a two-component epoxy resin (Loctite Hysol 9460). Overall, we fabricated more than 356 electrodes for our photoelectrochemical studies (Figure S23).

Each bare FTO working electrode area was coated with aqueous particle dispersions of the materials shown in Figure 1. We established that 20 μL of the aqueous dispersion covered our circular FTO area best. The 20 μL droplets of aqueous particle dispersions that contained 134 μg ZnO or 12.9 μg TiO_2, were dried for 5 min under an infrared heat lamp, followed by adding 5 μL of Nafion® solution (Sigma-Aldrich, 5 wt % Nafion® 117 solution in a mixture of lower aliphatic alcohols and water, diluted with water to obtain an active material to Nafion® mass ratio of 40/1), which was dried for 10 min under the heat lamp. We used a 1/1 mixture of as is and Na-exchanged Nafion® solution that we prepared according to ref. 130, to prevent ZnO and TiO2 corrosion by acidic un-exchanged Nafion®.

Photoelectrochemical performance data. Linear sweep voltammograms were measured in a standard one-compartment three-electrode cell fitted with a flat quartz window for illumination. The electrolytes were 0.1 M aqueous pH 7.0 sodium phosphate buffer or 0.1 M aqueous pH 7.0 sodium phosphate buffer with 0.5 M Na_2SO_3 as sacrificial hole acceptor. Phosphate buffer was prepared by dissolving 12 g of NaH_2PO_4 in 900 mL water and titrated with

HCl and NaOH until pH 7.0 (measured with a SympHony SB70P pH meter and a Thermo Scientific electrode model Orion 9102BNWP) was reached and then filled with water to 1 L. The counter electrode was nickel gauze (Alfa), and the reference electrode was a calibrated 3 M NaCl Ag/AgCl electrode (BASi). Currents were acquired with a Gamry 600 potentiostat at room temperature and in ambient air (scan rate 10 mV s^{-1}). Linear sweep voltammograms were obtained with rapid stirring of the liquid, to minimize mass transport effects and remove nucleated bubbles from the electrode surface; the data were not corrected for any uncompensated resistance losses.

We used an Oriel Instruments model 66902 halogen light source with an ozone-free bulb with an AM1.5G filter between the lamp and the photoelectrochemical cell to supply simulated sunlight. The light source was placed at a distance from the electrode surface such that an incident photon flux equivalent to 1 Sun illumination was achieved; the illumination intensity at the sample plane was measured to be 100 mW cm^{-2} by a calibrated Si photodiode (Thorlabs). Photocurrent values were averaged using three electrodes per sample, in electrolytes without or with sulfite, respectively; the given error bars are standard deviations. We obtained good reproducibility between electrodes. We acquired photoelectrochemical data without and with front-side illumination; photocurrents are the difference between light and dark currents.

ASSOCIATED CONTENT

Supporting Information. Photos of laser setups; energy conversion details; optical spectra; XRD data; PL data and simulations; fitting procedure details; linear sweep voltammograms; retrieval rate data; photo of electrodes; electron microscopy images. This material is available free of charge via the Internet at http://pubs.acs.org.

AUTHOR INFORMATION

Corresponding Authors

Stephan Barcikowski: stephan.barcikowski@uni-due.de
Astrid M. Müller: astrid.mueller@rochester.edu

Present Addresses

[§] TRUMPF Laser- und Systemtechnik GmbH, Johann-Maus-Straße 2, 71254 Ditzingen, Germany
[||] Institut für Mikroelektronik Stuttgart, Allmandring 30a, 70569 Stuttgart, Germany
[¶] Department of Chemical Engineering, University of Rochester, Rochester, New York 14627-0166

Author Contributions

M.L. and S.R. contributed equally to this work and both should be considered as the first author. All authors contributed to writing the manuscript and agreed on its final content.

Notes

The authors declare no competing financial interest.

ACKNOWLEDGMENT

We thank Prof. Dr. Hartmut Wiggers (University of Duisburg-Essen) for access to the photoluminescence spectrometer. We also gratefully acknowledge financial support from the European Regional Development Fund (Interreg Europe) that funded M.L. within the SAILPRO (Safe and Amplified Industrial Laser Processing) project, part of the ROCKET-Project (RegiOnal Collaboration on Key Enabling Technologies). S.R. thanks the Mercator Research Center Ruhr (MERCUR), Pr-2014-0044, and I.H. the German Federal Environmental Foundation (DBU). S.B. thanks the German Research Foundation for funding within CRC TRR 247. Research at the California Institute of Technology was carried out in the Molecular Materials Research Center of the Beckman Institute and was supported by the NSF CCI Solar Fuels Program (CHE-1305124) and the Arnold and Mabel Beckman Foundation.

ABBREVIATIONS

2D, two-dimensional; AuNP, gold nanoparticle; FTO, fluorine-doped tin oxide; HPLC, high-performance liquid chromatography; ICDD, International Centre for Diffraction Data; j_{ph}, photocurrent density; PAS, positron annihilation spectroscopy; PDF, powder diffraction file; PEC, photoelectrochemical; PL, photoluminescence; PLFL, pulsed laser fragmentation in liquids; PLML, pulsed laser melting in liquids; RHE, reversible hydrogen electrode; SEM, scanning electron microscopy; SMS, sub-micrometer spheres; SPR, surface plasmon resonance; ST, shallow trap; STE, self-trapped exciton; TEM, transmission electron microscopy; UV, ultraviolet; V, vacancy; wt, weight; XRD, X-ray diffraction.

REFERENCES

(1) Gray, H. B. Powering the Planet with Solar Fuel. *Nature Chem.* **2009**, *1*, 7.

(2) Hunter, B. M.; Gray, H. B.; Müller, A. M. Earth-abundant Heterogeneous Water Oxidation Catalysts. *Chem. Rev.* **2016**, *116*, 14120–14136.

(3) House, R. L.; Iha, N. Y. M.; Coppo, R. L.; Alibabaei, L.; Sherman, B. D.; Kang, P.; Brennaman, M. K.; Hoertz, P. G.; Meyer, T. J. Artificial Photosynthesis: Where Are We Now? Where Can We Go? *J. Photochem. Photobiol. C* **2015**, *25*, 32–45.

(4) Fujishima, A.; Honda, K. Electrochemical Photolysis of Water at a Semiconductor Electrode. *Nature* **1972**, *238*, 37–38.

(5) Hassan, N. K.; Hashim, M. R.; Allam, N. K. ZnO Nano-Tetrapod Photoanodes for Enhanced Solar-Driven Water Splitting. *Chem. Phys. Lett.* **2012**, *549*, 62–66.

(6) Bak, T.; Nowotny, J.; Rekas, M.; Sorrell, C. Photo-electrochemical Hydrogen Generation from Water Using Solar Energy. Materials-Related Aspects. *Int. J. Hydrogen Energy* **2002**, *27*, 991–1022.

(7) Zhang, J.; Zhang, L.; Zhang, J.; Zhang, Z.; Wu, Z. Effect of Surface/Bulk Oxygen Vacancies on the Structure and Electrochemical Performance of TiO2 Nanoparticles. *J. Alloys Compd.* **2015**, *642*, 28–33.

(8) Zhang, J.; Zhang, J.; Ren, H.; Yu, L.; Wu, Z.; Zhang, Z. High Rate Capability and Long Cycle Stability of TiO2- δ–La Composite Nanotubes as Anode Material for Lithium Ion Batteries. *J. Alloys Compd.* **2014**, *609*, 178–184.

(9) Ishikawa, Y.; Koshizaki, N.; Pyatenko, A.; Saitoh, N.; Yoshizawa, N.; Shimizu, Y. Nano-and Submicrometer-Sized Spherical Particle Fabrication Using a Submicroscopic Droplet Formed Using Selective Laser Heating. *J. Phys. Chem. C* **2016**, *120*, 2439–2446.

(10) Lau, M.; Ziefuss, A.; Komossa, T.; Barcikowski, S. Inclusion of Supported Gold Nanoparticles into Their Semiconductor Support. *Phys. Chem. Chem. Phys.* **2015**, *17*, 29311–29318.

(11) Lau, M.; Barcikowski, S. Quantification of Mass-Specific Laser Energy Input Converted into Particle Properties During Picosecond Pulsed Laser Fragmentation of Zinc Oxide and Boron Carbide in Liquids. *Appl. Surf. Sci.* **2015**, *348*, 22–29.

(12) Qiu, J.; Zeng, G.; Pavaskar, P.; Li, Z.; Cronin, S. B. Plasmon-enhanced Water Splitting on TiO2-Passivated GaP Photocatalysts. *Phys. Chem. Chem. Phys.* **2014**, *16*, 3115–3121.

(13) Hung, W.-H.; Yang, K.-L.; Lai, S.-N.; Yang, C.-R.; Shyue, J.-J.; Ku, C.-S.; Cronin, S. B. Demonstration of Enhanced Carrier Transport, Charge Separation, and Long-Term Stability for Photocatalytic Water Splitting by a Rapid Hot Pressing Process. *J. Mater. Chem. A* **2017**, *5*, 10687–10695.

(14) Lamberti, F.; Litti, L.; De Bastiani, M.; Sorrentino, R.; Gandini, M.; Meneghetti, M.; Petrozza, A. High-Quality, Ligands-Free, Mixed-

Halide Perovskite Nanocrystals Inks for Optoelectronic Applications. *Adv. Energy Mater.* **2017**, *7*, 1601703-1–5.

(15) Zhang, D.; Gökce, B.; Barcikowski, S. Laser Synthesis and Processing of Colloids: Fundamentals and Applications. *Chem. Rev.* **2017**, *117*, 3990–4103.

(16) Blakemore, J. D.; Gray, H. B.; Winkler, J. R.; Müller, A. M. Co3O4 Nanoparticle Water-Oxidation Catalysts Made by Pulsed-Laser Ablation in Liquids. *ACS Catal.* **2013**, *3*, 2497–2500.

(17) Hunter, B. M.; Blakemore, J. D.; Deimund, M.; Gray, H. B.; Winkler, J. R.; Müller, A. M. Highly Active Mixed-Metal Nanosheet Water Oxidation Catalysts Made by Pulsed-Laser Ablation in Liquids. *J. Am. Chem. Soc.* **2014**, *136*, 13118–13121.

(18) Blumenfeld, C. M.; Lau, M.; Gray, H. B.; Müller, A. M. Mixed-Metal Tungsten Oxide Photoanode Materials Made by Pulsed-Laser in Liquids Synthesis. *ChemPhysChem* **2017**, *18*, 1091–1100.

(19) Roske, C. W.; Lefler, J. W.; Müller, A. M. Complex Nanomineral Formation Utilizing Kinetic Control by PLAL. *J. Coll. Interf. Sci.* **2017**, *489*, 68–75.

(20) Lau, M.; Niemann, R. G.; Bartsch, M.; O'Neill, W.; Barcikowski, S. Near-Field-Enhanced, Off-Resonant Laser Sintering of Semiconductor Particles for Additive Manufacturing of Dispersed Au–ZnO-Micro/Nano Hybrid Structures. *Appl. Phys. A* **2014**, *114*, 1023–1030.

(21) Amendola, V.; Meneghetti, M. What Controls the Composition and the Structure of Nanomaterials Generated by Laser Ablation in Liquid Solution? *Phys. Chem. Chem. Phys.* **2013**, *15*, 3027–3046.

(22) Filice, S.; Compagnini, G.; Fiorenza, R.; Sciré, S.; D'Urso, L.; Fragalá, M. E.; Russo, P.; Fazio, E.; Scalese, S. Laser Processing of TiO2 Colloids for an Enhanced Photocatalytic Water Splitting Activity. *J. Coll. Interf. Sci.* **2017**, *489*, 131–137.

(23) Chen, X.; Zhao, D.; Liu, K.; Wang, C.; Liu, L.; Li, B.; Zhang, Z.; Shen, D. Laser-Modified Black Titanium Oxide Nanospheres and Their Photocatalytic Activities under Visible Light. *ACS Appl. Mater. Interfaces* **2015**, *7*, 16070–16077.

(24) Ishikawa, Y.; Shimizu, Y.; Sasaki, T.; Koshizaki, N. Boron Carbide Spherical Particles Encapsulated in Graphite Prepared by Pulsed Laser Irradiation of Boron in Liquid Medium. *Appl. Phys. Lett.* **2007**, *91*, 161110-1–3.

(25) Wang, H.; Pyatenko, A.; Kawaguchi, K.; Li, X.; SwiatkowskaWarkocka, Z.; Koshizaki, N. Selective Pulsed Heating for the Synthesis of Semiconductor and Metal Submicrometer Spheres. *Angew. Chem. Int. Ed.* **2010**, *49*, 6361–6364.

(26) Wang, H.; Koshizaki, N.; Li, L.; Jia, L.; Kawaguchi, K.; Li, X.; Pyatenko, A.; SwiatkowskaWarkocka, Z.; Bando, Y.; Golberg, D. Size-Tailored ZnO Submicrometer Spheres: Bottom-Up Construction, Size-Related Optical Extinction, and Selective Aniline Trapping. *Adv. Mater.* **2011**, *23*, 1865–1870.

(27) Zhang, D.; Lau, M.; Lu, S.; Barcikowski, S.; Gökce, B. Germanium Sub-Microspheres Synthesized by Picosecond Pulsed Laser Melting in Liquids: Educt Size Effects. *Sci. Rep.* **2017**, *7*, 40355-1–11.

(28) Sakaki, S.; Ikenoue, H.; Tsuji, T.; Ishikawa, Y.; Koshizaki, N. Pulse-Width Dependence of the Cooling Effect on Sub-Micrometer ZnO Spherical Particle Formation by Pulsed-Laser Melting in a Liquid. *ChemPhysChem* **2017**, *18*, 1101–1107.

(29) Sakaki, S.; Saitow, K.-i.; Sakamoto, M.; Wada, H.; Swiatkowska-Warkocka, Z.; Ishikawa, Y.; Koshizaki, N. Comparison of Picosecond and Nanosecond Lasers for the Synthesis of TiN Sub-Micrometer Spherical Particles by Pulsed Laser Melting in Liquid. *Appl. Phys. Express* **2018**, *11*, 035001-1–4.

(30) Strasser, M.; Setoura, K.; Langbein, U.; Hashimoto, S. Computational Modeling of Pulsed Laser-Induced Heating and Evaporation of Gold Nanoparticles. *J. Phys. Chem. C* **2014**, *118*, 25748–25755.

(31) Sundaram, S.; Mazur, E. Inducing and Probing Non-Thermal Transitions in Semiconductors Using Femtosecond Laser Pulses. *Nat. Mater.* **2002**, *1*, 217–224.

(32) Yan, J.; Wu, G.; Guan, N.; Li, L.; Li, Z.; Cao, X. Understanding the Effect of Surface/Bulk Defects on the Photocatalytic Activity of TiO2: Anatase versus Rutile. *Phys. Chem. Chem. Phys.* **2013**, *15*, 10978–10988.

(33) Nowotny, J.; Bak, T.; Nowotny, M.; Sheppard, L. TiO2 Surface Active Sites for Water Splitting. *J. Phys. Chem. B* **2006**, *110*, 18492–18495.

(34) Khan, S. U.; Al-Shahry, M.; Ingler, W. B. Efficient Photochemical Water Splitting by a Chemically Modified n-TiO2. *Science* **2002**, *297*, 2243–2245.

(35) Yang, X.; Wolcott, A.; Wang, G.; Sobo, A.; Fitzmorris, R. C.; Qian, F.; Zhang, J. Z.; Li, Y. Nitrogen-Doped ZnO Nanowire Arrays for Photoelectrochemical Water Splitting. *Nano Lett.* **2009**, *9*, 2331–2336.

(36) Mohapatra, S. K.; Misra, M.; Mahajan, V. K.; Raja, K. S. Design of a Highly Efficient Photoelectrolytic Cell for Hydrogen Generation by Water Splitting: Application of $TiO_{2-x}C_x$ Nanotubes as a Photoanode and Pt/TiO_2 Nanotubes as a Cathode. *J. Phys. Chem. C* **2007**, *111*, 8677–8685.

(37) Wang, G.; Wang, H.; Ling, Y.; Tang, Y.; Yang, X.; Fitzmorris, R. C.; Wang, C.; Zhang, J. Z.; Li, Y. Hydrogen-Treated TiO2 Nanowire Arrays for Photoelectrochemical Water Splitting. *Nano Lett.* **2011**, *11*, 3026–3033.

(38) Aggelopoulos, C. A.; Dimitropoulos, M.; Govatsi, A.; Sygellou, L.; Tsakiroglou, C. D.; Yannopoulos, S. N. Influence of the Surface-to-Bulk Defects Ratio of ZnO and TiO2 on their UV-Mediated Photocatalytic Activity. *Appl. Catal. B* **2017**, *205*, 292–301.

(39) Zhang, Z.; Zhang, L.; Hedhili, M. N.; Zhang, H.; Wang, P. Plasmonic Gold Nanocrystals Coupled with Photonic Crystal Seamlessly on TiO2 Nanotube Photoelectrodes for Efficient Visible Light Photoelectrochemical Water Splitting. *Nano Lett.* **2012**, *13*, 14–20.

(40) Pu, Y. C.; Wang, G.; Chang, K. D.; Ling, Y.; Lin, Y. K.; Fitzmorris, B. C.; Liu, C. M.; Lu, X.; Tong, Y.; Zhang, J. Z. Au Nanostructure-Decorated TiO2 Nanowires Exhibiting Photoactivity Across Entire UV-Visible Region for Photoelectrochemical Water Splitting. *Nano Lett.* **2013**, *13*, 3817–3823.

(41) Priebe, J. B.; Karnahl, M.; Junge, H.; Beller, M.; Hollmann, D.; Brückner, A. Water Reduction with Visible Light: Synergy Between Optical Transitions and Electron Transfer in Au-TiO2 Catalysts Visualized by In Situ EPR Spectroscopy. *Angew. Chem. Int. Ed.* **2013**, *52*, 11420–11424.

(42) Kushwaha, A.; Aslam, M. Defect Controlled Water Splitting Characteristics of Gold Nanoparticle Functionalized ZnO Nanowire Films. *RSC Adv.* **2014**, *4*, 20955–20963.

(43) Tang, J.; Durrant, J. R.; Klug, D. R. Mechanism of Photocatalytic Water Splitting in TiO2. Reaction of Water with Photoholes, Importance of Charge Carrier Dynamics, and Evidence for Four-Hole Chemistry. *J. Am. Chem. Soc.* **2008**, *130*, 13885–13891.

(44) Osterloh, F. E. *Solar Energy for Fuels*; Springer, 2015; pp 105–142.

(45) Grätzel, M. Photoelectrochemical Cells. *Nature* **2001**, *414*, 338–344.

(46) Guijarro, N.; Prévot, M. S.; Sivula, K. Surface Modification of Semiconductor Photoelectrodes. *Phys. Chem. Chem. Phys.* **2015**, *17*, 15655–15674.

(47) Hou, B.; Rezaeifar, F.; Qiu, J.; Zeng, G.; Kapadia, R.; Cronin, S. B. Prevention of Surface Recombination by Electrochemical Tuning of TiO2-Passivated Photocatalysts. *Appl. Phys. Lett.* **2017**, *111*, 141603-1–6.

(48) Cao, F.; Oskam, G.; Searson, P. C.; Stipkala, J. M.; Heimer, T. A.; Farzad, F.; Meyer, G. J. Electrical and Optical Properties of Porous Nanocrystalline TiO2 Films. *J. Phys. Chem.* **1995**, *99*, 11974–11980.

(49) Cho, I. S.; Chen, Z.; Forman, A. J.; Kim, D. R.; Rao, P. M.; Jaramillo, T. F.; Zheng, X. Branched TiO2 Nanorods for Photoelectrochemical Hydrogen Production. *Nano Lett.* **2011**, *11*, 4978–4984.

(50) Voepel, P.; Weiss, M.; Smarsly, B. M.; Marschall, R. Photocatalytic Activity of Multiphase TiO2 (B) / Anatase Nanoparticle Heterojunctions Prepared from Ionic Liquids. *J. Photochem. Photobiol. A* **2018**, *in press*.

(51) Whitaker, K. M.; Ochsenbein, S. T.; Polinger, V. Z.; Gamelin, D. R. Electron Confinement Effects in the EPR Spectra of Colloidal n-type ZnO Quantum Dots. *J. Phys. Chem. C* **2008**, *112*, 14331–14335.

(52) Jovic, V.; Chen, W.-T.; Sun-Waterhouse, D.; Blackford, M. G.; Idriss, H.; Waterhouse, G. I. Effect of Gold Loading and TiO2 Support Composition on the Activity of Au/TiO2 Photocatalysts for H2 Production from Ethanol-Water Mixtures. *J. Catal.* **2013**, *305*, 307–317.

(53) Özgür, Ü.; Alivov, Y. I.; Liu, C.; Teke, A.; Reshchikov, M.; Dogăn, S.; Avrutin, V.; Cho, S.-J.; Morkoc, H. A Comprehensive Review of ZnO Materials and Devices. *J. Appl. Phys.* **2005**, *98*, 041301.

(54) Ashrafi, A.; Jagadish, C. Review of Zincblende ZnO: Stability of Metastable ZnO Phases. *J. Appl. Phys.* **2007**, *102*, 071101-1–13.

(55) Honda, M.; Goto, T.; Owashi, T.; Rozhin, A. G.; Yamaguchi, S.; Ito, T.; Kulinich, S. A. ZnO Nanorods Prepared via Ablation of Zn with Millisecond Laser in Liquid Media. *Phys. Chem. Chem. Phys.* **2016**, *18*, 23628–23637.

(56) Yoshida, T.; Tachibana, T.; Maemoto, T.; Sasa, S.; Inoue, M. Pulsed Laser Deposition of ZnO Grown on Glass Substrates for Realizing High-Performance Thin-Film Transistors. *Appl. Phys. A* **2010**, *101*, 685–688.

(57) Cetinkaya, C.; Peri, M. M. Non-Contact Nanoparticle Removal with Laser Induced Plasma Pulses. *Nanotechnology* **2004**, *15*, 435–440.

(58) Zhou, D.; Cetinkaya, C. Molecular-Level Mechanisms of Nanoparticle Detachment in Laser-Induced Plasma Shock Waves. *Appl. Phys. Lett.* **2006**, *88*, 173109-1–3.

(59) Mittal, K.; Lei, W.-S. *Laser Technology: Applications in Adhesion and Related Areas*; John Wiley & Sons, 2018.

(60) Werner, D.; Hashimoto, S. Improved Working Model for Interpreting the Excitation Wavelength and Fluence-Dependent Response in Pulsed Laser-Induced Size Reduction of Aqueous Gold Nanoparticles. *J. Phys. Chem. C* **2010**, *115*, 5063–5072.

(61) Hashimoto, S.; Werner, D.; Uwada, T. Studies on the Interaction of Pulsed Lasers with Plasmonic Gold Nanoparticles Toward Light Manipulation, Heat Management, and Nanofabrication. *J. Photochem. Photobiol. C* **2012**, *13*, 28–54.

(62) Lau, M.; Haxhiaj, I.; Wagener, P.; Intartaglia, R.; Brandi, F.; Nakamura, J.; Barcikowski, S. Ligand-free Gold Atom Clusters Adsorbed on Graphene Nano Sheets Generated by Oxidative Laser Fragmentation in Water. *Chem. Phys. Lett.* **2014**, *610*, 256–260.

(63) Zhang, D.; Ushita, H.; Wang, P.; Park, C.; Murakami, R.-i.; Yang, S.-c.; Song, X. Photoluminescence Modulation of ZnO via Coupling with the Surface Plasmon Resonance of Gold Nanoparticles. *Appl. Phys. Lett.* **2013**, *103*, 093114-1–5.

(64) Guidelli, E.; Baffa, O.; Clarke, D. Enhanced UV Emission from Silver/ZnO and Gold/ZnO Core-Shell Nanoparticles: Photoluminescence, Radioluminescence, and Optically Stimulated Luminescence. *Sci. Rep.* **2015**, *5*, 14004-1–11.

(65) Im, J.; Singh, J.; Soares, J. W.; Steeves, D. M.; Whitten, J. E. Synthesis and Optical Properties of Dithiol-Linked ZnO/Gold Nanoparticle Composites. *J. Phys. Chem. C* **2011**, *115*, 10518–10523.

(66) Ruiz Peralta, M. D. L.; Pal, U.; Zeferino, R. S. Photoluminescence (PL) Quenching and Enhanced Photocatalytic Activity of Au-decorated ZnO Nanorods Fabricated Through Microwave-Assisted Chemical Synthesis. *ACS Appl. Mater. Interfaces* **2012**, *4*, 4807–4816.

(67) Janotti, A.; Van de Walle, C. G. Native Point Defects in ZnO. *Phys. Rev. B* **2007**, *76*, 165202-1–22.

(68) Kaftelen, H.; Ocakoglu, K.; Thomann, R.; Tu, S.; Weber, S.; Erdem, E. EPR and Photoluminescence Spectroscopy Studies on the Defect Structure of ZnO Nanocrystals. *Phys. Rev. B* **2012**, *86*, 014113-1–9.

(69) Wang, Z.; Su, S.; Younas, M.; Ling, F.; Anwand, W.; Wagner, A. The Zn-Vacancy Related Green Luminescence and Donor–Acceptor Pair Emission in ZnO Grown by Pulsed Laser Deposition. *RSC Adv.* **2015**, *5*, 12530–12535.

(70) Garces, N.; Wang, L.; Bai, L.; Giles, N.; Halliburton, L.; Cantwell, G. Role of Copper in the Green Luminescence from ZnO Crystals. *Appl. Phys. Lett.* **2002**, *81*, 622–624.

(71) Leiter, F.; Alves, H.; Pfisterer, D.; Romanov, N.; Hofmann, D.; Meyer, B. Oxygen Vacancies in ZnO. *Physica B* **2003**, *340*, 201–204.

(72) Meng, X.; Shen, D.; Zhang, J.; Zhao, D.; Lu, Y.; Dong, L.; Zhang, Z.; Liu, Y.; Fan, X. The Structural and Optical Properties of ZnO Nanorod Arrays. *Solid State Commun.* **2005**, *135*, 179–182.

(73) Djurišic, A. B.; Leung, Y. H. Optical Properties of ZnO Nanostructures. *Small* **2006**, *2*, 944–961.

(74) Fabbri, F.; Villani, M.; Catellani, A.; Calzolari, A.; Cicero, G.; Calestani, D.; Calestani, G.; Zappettini, A.; Dierre, B.; Sekiguchi, T.; Salviati, G. Zn Vacancy Induced Green Luminescence on Non-Polar Surfaces in ZnO Nanostructures. *Sci. Rep.* **2014**, *4*, 5158-1–6.

(75) Børseth, T. M.; Svensson, B.; Kuznetsov, A. Y.; Klason, P.; Zhao, Q.; Willander, M. Identification of Oxygen and Zinc Vacancy Optical Signals in ZnO. *Appl. Phys. Lett.* **2006**, *89*, 262112-1–3.

(76) Erhart, P.; Klein, A.; Albe, K. First-principles Study of the Structure and Stability of Oxygen Defects in Zinc Oxide. *Phys. Rev. B* **2005**, *72*, 085213-1–7.

(77) Streubel, R.; Bendt, G.; Gökce, B. Pilot-Scale Synthesis of Metal Nanoparticles by High-Speed Pulsed Laser Ablation in Liquids. *Nanotechnology* **2016**, *27*, 205602-1–9.

(78) Fischer, M.; Hormes, J.; Marzun, G.; Wagener, P.; Hagemann, U.; Barcikowski, S. In Situ Investigations of Laser-Generated Ligand-Free Platinum Nanoparticles by X-ray Absorption Spectroscopy: How Does the Immediate Environment Influence the Particle Surface? *Langmuir* **2016**, *32*, 8793–8802.

(79) Bora, T.; Kyaw, H. H.; Sarkar, S.; Pal, S. K.; Dutta, J. Highly Efficient ZnO/Au Schottky Barrier Dye-sensitized Solar Cells: Role of Gold Nanoparticles on the Charge-Transfer Process. *Beilstein J. Nanotechnol.* **2011**, *2*, 681–690.

(80) Huang, G.-Y.; Wang, C.-Y.; Wang, J.-T. First-Principles Study of Diffusion of Zinc Vacancies and Interstitials in ZnO. *Solid State Commun.* **2009**, *149*, 199–204.

(81) Tuomisto, F.; Saarinen, K.; Look, D. C.; Farlow, G. C. Introduction and Recovery of Point Defects in Electron-Irradiated ZnO. *Phys. Rev. B* **2005**, *72*, 085206-1–11.

(82) Jeong, I.-S.; Kim, J. H.; Im, S. Ultraviolet-Enhanced Photodiode Employing n-ZnO/p-Si Structure. *Appl. Phys. Lett.* **2003**, *83*, 2946–2948.

(83) Lakowicz, J. R. Radiative Decay Engineering 5: Metal-Enhanced Fluorescence and Plasmon Emission. *Anal. Biochem.* **2005**, *337*, 171–194.

(84) Lam, J.; Amans, D.; Chaput, F.; Diouf, M.; Ledoux, G.; Mary, N.; Masenelli-Varlot, K.; Motto-Ros, V.; Dujardin, C. γ-Al2O3 Nanoparticles Synthesised by Pulsed Laser Ablation in Liquids: a Plasma Analysis. *Phys. Chem. Chem. Phys.* **2014**, *16*, 963–973.

(85) Norberg, N. S.; Gamelin, D. R. Influence of Surface Modification on the Luminescence of Colloidal ZnO Nanocrystals. *J. Phys. Chem. B* **2005**, *109*, 20810–20816.

(86) Kavitha, M. K.; Jinesh, K. B.; Philip, R.; Gopinath, P.; John, H. Defect Engineering in ZnO Nanocones for Visible Photoconductivity and Nonlinear Absorption. *Phys. Chem. Chem. Phys.* **2014**, *16*, 25093–25100.

(87) Yoshikawa, H.; Adachi, S. Optical Constants of ZnO. *Jpn. J. Appl. Phys.* **1997**, *36*, 6237–6243.

(88) Park, J. Y.; Lee, H.; Renzas, J. R.; Zhang, Y.; Somorjai, G. A. Probing Hot Electron Flow Generated on Pt Nanoparticles with Au/TiO2 Schottky Diodes During Catalytic CO Oxidation. *Nano Lett.* **2008**, *8*, 2388–2392.

(89) Kim, S. M.; Lee, S. W.; Moon, S. Y.; Park, J. Y. The Effect of Hot Electrons and Surface Plasmons on Heterogeneous Catalysis. *J. Phys. Condens. Matter* **2016**, *28*, 254002-1–13.

(90) Xu, Z.; Quintanilla, M.; Vetrone, F.; Govorov, A. O.; Chaker, M.; Ma, D. Harvesting Lost Photons: Plasmon and Upconversion Enhanced Broadband Photocatalytic Activity in Core@Shell Microspheres Based on Lanthanide-Doped NaYF4, TiO2, and Au. *Adv. Funct. Mater.* **2015**, *25*, 2950–2960.

(91) Zhukov, V.; Tyuterev, V. G.; Chulkov, E. V. Electron–Phonon Relaxation and Excited Electron Distribution in Zinc Oxide and Anatase. *J. Phys. Condens. Matter* **2012**, *24*, 405802-1–10.

(92) Pougin, A.; Lüken, A.; Klinkhammer, C.; Hiltrop, D.; Kauer, M.; Tölle, K.; Havenith-Newen, M.; Morgenstern, K.; Grünert, W.; Muhler, M.; Strunk, J. Probing Oxide Reduction and Phase Transformations at the Au-TiO2 Interface by Vibrational Spectroscopy. *Top. Catal.* **2017**, *60*, 1744–1753.

(93) Ohtani, B.; Prieto-Mahaney, O.; Li, D.; Abe, R. What is Degussa (Evonik) P25? Crystalline Composition Analysis, Reconstruction from Isolated Pure Particles and Photocatalytic Activity Test. *J. Photochem. Photobiol. A* **2010**, *216*, 179–182.

(94) Hanaor, D. A.; Sorrell, C. C. Review of the Anatase to Rutile Phase Transformation. *J. Mater. Sci.* **2011**, *46*, 855–874.

(95) Luttrell, T.; Halpegamage, S.; Tao, J.; Kramer, A.; Sutter, E.; Batzill, M. Why is Anatase a Better Photocatalyst than Rutile? Model Studies on Epitaxial TiO2 Films. *Sci. Rep.* **2014**, *4*, 4043-1–8.

(96) Tang, H.; Su, Y.; Zhang, B.; Lee, A. F.; Isaacs, M. A.; Wilson, K.; Li, L; Ren, Y.; Huang, J; Haruta, M.; Qiao, B.; Liu, X.; Jin, C.; Su, D.; Wang, J.; Zhang, T. Classical Strong Metal–Support Interactions Between Gold Nanoparticles and Titanium Dioxide. *Sci. Adv.* **2017**, *3*, e1700231-1–8.

(97) Zou, L.; Yang, C.; Lei, Y.; Zakharov, D.; Wiezorek, J. M.; Su, D.; Yin, Q.; Li, J.; Liu, Z.; Stach, E. A.; Yang, J. C.; Qi, L.; Wang, G.; Zhou, G. Dislocation Nucleation Facilitated by Atomic Segregation. *Nat. Mater.* **2018**, *17*, 56–63.

(98) Jellison Jr, G.; Boatner, L.; Budai, J.; Jeong, B.-S.; Norton, D. Spectroscopic Ellipsometry of Thin Film and Bulk Anatase (TiO2). *J. Appl. Phys.* **2003**, *93*, 9537–9541.

(99) Serpone, N.; Lawless, D.; Khairutdinov, R. Size Effects on the Photophysical Properties of Colloidal Anatase TiO2 Particles: Size Quantization versus Direct Transitions in this Indirect Semiconductor? *J. Phys. Chem. C* **1995**, *99*, 16646–16654.

(100) Stevanovic, A.; Büttner, M.; Zhang, Z.; Yates Jr, J. T. Photoluminescence of TiO2: Effect of UV Light and Adsorbed Molecules on Surface Band Structure. *J. Am. Chem. Soc.* **2012**, *134*, 324–332.

(101) Knorr, F. J.; Zhang, D.; McHale, J. L. Influence of TiCl4 Treatment on Surface Defect Photoluminescence in Pure and Mixed-Phase Nanocrystalline TiO2. *Langmuir* **2007**, *23*, 8686–8690.

(102) Chu, S.; Becerikli, A. E.; Kortewille, B.; Oropeza, F. E.; Strunk, J. Tin-Grafted TiO2 with Enhanced Activity for Photocatalytic Hydrogen Generation from Aqueous Methanol Solutions. *Int. J. Hydrogen Energy* **2014**, *39*, 18784–18792.

(103) Kunti, A. K.; Sekhar, K.; Pereira, M.; Gomes, M.; Sharma, S. K. Oxygen Partial Pressure Induced Effects on the Microstructure and the Luminescence Properties of Pulsed Laser Deposited TiO2 Thin Films. *AIP Adv.* **2017**, *7*, 015021-1–8.

(104) Song, X.; Gao, L. Synthesis, Characterization, and Optical Properties of Well-Defined N-Doped, Hollow Silica/Titania Hybrid Microspheres. *Langmuir* **2007**, *23*, 11850–11856.

(105) Horn, M.; Schwerdtfeger, C.; Meagher, E. Refinement of the Structure of Anatase at Several Temperatures. *Z. Kristallogr. Cryst. Mater.* **1972**, *136*, 273–281.

(106) Swope, R. J.; Smyth, J. R.; Larson, A. C. H in Rutile-type Compounds: I. Single-crystal Neutron and X-ray Diffraction Study of H in Rutile. *Am. Mineral.* **1995**, *80*, 448–453.

(107) Cheng, H.; Selloni, A. Surface and Subsurface Oxygen Vacancies in Anatase TiO2 and Differences with Rutile. *Phys. Rev. B* **2009**, *79*, 092101-1–4.

(108) Diebold, U. The Surface Science of Titanium Dioxide. *Surf. Sci. Rep.* **2003**, *48*, 53–229.

(109) Li, H.; Guo, Y.; Robertson, J. Calculation of TiO2 Surface and Subsurface Oxygen Vacancy by the Screened Exchange Functional. *J. Phys. Chem. C* **2015**, *119*, 18160–18166.

(110) Bonapasta, A. A.; Filippone, F.; Mattioli, G.; Alippi, P. Oxygen Vacancies and OH Species in Rutile and Anatase TiO2 Polymorphs. *Catal. Today* **2009**, *144*, 177–182.

(111) Attwood, A.; Murphy, D.; Edwards, J.; Egerton, T.; Harrison, R. An EPR study of Thermally and Photochemically Generated Oxygen Radicals on Hydrated and Dehydrated Titania Surfaces. *Res. Chem. Intermed.* **2003**, *29*, 449–465.

(112) Murphy, D. M.; Chiesa, M. In *Electron Paramagnetic Resonance: Volume 19*; Gilbert, B. C., Davies, M. J., Murphy, D. M., Eds.; The Royal Society of Chemistry, 2004; Vol. 19; pp 279–317.

(113) Carter, E.; Carley, A. F.; Murphy, D. M. Evidence for O2- Radical Stabilization at Surface Oxygen Vacancies on Polycrystalline TiO2. *J. Phys. Chem. C* **2007**, *111*, 10630–10638.

(114) Xiong, L.-B.; Li, J.-L.; Yang, B.; Yu, Y. Ti3+ in the Surface of Titanium Dioxide: Generation, Properties and Photocatalytic Application. *J. Nanomater.* **2012**, *2012*, 9-1–13.

(115) Amano, F.; Nakata, M.; Yamamoto, A.; Tanaka, T. Effect of Ti3+ Ions and Conduction Band Electrons on Photocatalytic and Photoelectrochemical Activity of Rutile Titania for Water Oxidation. *J. Phys. Chem. C* **2016**, *120*, 6467–6474.

(116) Zywitzki, D.; Jing, H.; Tüysüz, H.; Chan, C. K. High Surface Area, Amorphous Titania with Reactive Ti3+ Through a Photo-Assisted Synthesis Method for Photocatalytic H2 Generation. *J. Mater. Chem. A* **2017**, *5*, 10957–10967.

(117) Kavan, L.; Grätzel, M.; Gilbert, S.; Klemenz, C.; Scheel, H. Electrochemical and Photoelectrochemical Investigation of Single-crystal Anatase. *J. Am. Chem. Soc.* **1996**, *118*, 6716–6723.

(118) Tang, H.; Levy, F.; Berger, H.; Schmid, P. Urbach Tail of Anatase TiO2. *Phys. Rev. B* **1995**, *52*, 7771–7774.

(119) Pascual, J.; Camassel, J.; Mathieu, H. Fine Structure in the Intrinsic Absorption Edge of TiO2. *Phys. Rev. B* **1978**, *18*, 5606–5614.

(120) Amtout, A.; Leonelli, R. Optical Properties of Rutile Near its Fundamental Band Gap. *Phys. Rev. B* **1995**, *51*, 6842–6851.

(121) Farnesi Camellone, M.; Zhao, J.; Jin, L.; Wang, Y.; Muhler, M.; Marx, D. Molecular Understanding of Reactivity and Selectivity for Methanol Oxidation at the Au/TiO2 Interface. *Angew. Chem. Int. Ed.* **2013**, *52*, 5780–5784.

(122) Kernazhitsky, L.; Shymanovska, V.; Gavrilko, T.; Naumov, V.; Fedorenko, L.; Kshnyakin, V.; Baran, J. Room Temperature Photoluminescence of Anatase and Rutile TiO2 Powders. *J. Lumin.* **2014**, *146*, 199–204.

(123) Schaub, R.; Thostrup, P.; Lopez, N.; Lægsgaard, E.; Stensgaard, I.; Nørskov, J. K.; Besenbacher, F. Oxygen Vacancies as Active Sites for Water Dissociation on Rutile TiO2 (110). *Phys. Rev. Lett.* **2001**, *87*, 266104-1–4.

(124) Romero-Sarria, F.; Plata, J.; Laguna, O.; Márquez, A.; Centeno, M.; Sanz, J. F.; Odriozola, J. Surface Oxygen Vacancies in Gold Based Catalysts for CO Oxidation. *RSC Adv.* **2014**, *4*, 13145–13152.

(125) Kihara, K.; Donnay, G. Anharmonic Thermal Vibrations in ZnO. *Can. Mineral.* **1985**, *23*, 647–654.

(126) Sinclair, T. S.; Gray, H. B.; Müller, A. M. Photoelectrochemical Performance of BiVO4 Photoanodes Integrated with [NiFe]-Layered Double Hydroxide Nanocatalysts. *Eur. J. Inorg. Chem.* **2018**, *2018*, 1060–1067.

(127) Sinclair, T. S.; Hunter, B. M.; Winkler, J. R.; Gray, H. B.; Müller, A. M. Factors Affecting Bismuth Vanadate Photoelectrochemical Performance. *Mater. Horiz.* **2015**, *2*, 330–337.

(128) Wang, H.; Lau, M.; Sannomiya, T.; Gökce, B.; Barcikowski, S.; Odawara, O.; Wada, H. Laser-Induced Growth of YVO4:Eu3+ Nanoparticles from Sequential Flowing Aqueous Suspension. *RSC Adv.* **2017**, *7*, 9002–9008.

(129) Lau, M.; Straube, T.; Aggarwal, A. V.; Hagemann, U.; de-Oliveira Viestel, B.; Hartmann, N.; Textor, T.; Lutz, H.; Gutmann, J. S.; Barcikowski, S. Gradual Modification of ITO Particle's Crystal Structure and Optical Properties by Pulsed UV Laser Irradiation in a Free Liquid Jet. *Dalton Trans.* **2017**, *46*, 6039–6048.

(130) Suntivich, J.; Gasteiger, H. A.; Yabuuchi, N.; Shao-Horn, Y. Electrocatalytic Measurement Methodology of Oxide Catalysts Using a Thin-Film Rotating Disk Electrode. *J. Electrochem. Soc.* **2010**, *157*, B1263–B1268.

Table of Contents (TOC) graphic.